PHYSICAL REVIEW B **81**, 024414 (2010)

Raman signature of the U(1) Dirac spin-liquid state in the spin-$\frac{1}{2}$ kagome system

Wing-Ho Ko,[1] Zheng-Xin Liu,[2] Tai-Kai Ng,[2] and Patrick A. Lee[1]
[1]*Department of Physics, Massachusetts Institute of Technology, Cambridge, Massachusetts 02139, USA*
[2]*Department of Physics, Hong Kong University of Science and Technology, Hong Kong, People's Republic of China*
(Received 4 November 2009; published 21 January 2010)

We followed the Shastry-Shraiman formulation of Raman scattering in Hubbard systems and considered the Raman intensity profile in the spin-$\frac{1}{2}$ "perfect" kagome lattice herbertsmithite $ZnCu_3(OH)_6Cl_2$, assuming the ground state is well-described by the U(1) Dirac spin-liquid state. In the derivation of the Raman T matrix, we found that the spin-chirality term appears in the A_{2g} channel in the kagome lattice at the $t^4/(\omega_i - U)^3$ order, but (contrary to the claims by Shastry and Shraiman) vanishes in the square lattice to that order. In the ensuing calculations on the spin-$\frac{1}{2}$ kagome lattice, we found that the Raman intensity profile in the E_g channel is invariant under an arbitrary rotation in the kagome plane, and that in all (A_{1g}, E_g, and A_{2g}) symmetry channels the Raman intensity profile contains broad continua that display power-law behaviors at low energy, with exponent approximately equal to 1 in the A_{2g} channel and exponent approximately equal to 3 in the E_g and the A_{1g} channels. For the A_{2g} channel, the Raman profile also contains a characteristic $1/\omega$ singularity, which arose in our model from an excitation of the emergent U(1) gauge field.

DOI: 10.1103/PhysRevB.81.024414 PACS number(s): 75.10.Jm, 75.40.Gb

I. INTRODUCTION

Quantum spin liquids, which are quantum ground states of interacting spin systems that break no symmetries, have long been a fascination among the theoretical condensed-matter community. After years of experimental searches, several promising candidates finally emerged, including the "perfect" spin-$\frac{1}{2}$ kagome lattice herbertsmithite $ZnCu_3(OH)_6Cl_2$, which shows no signs of magnetic ordering down to a temperature of 50 mK, despite having a nearest-neighbor antiferromagnetic exchange $J \approx 190$ K.[1–3]

Ever since the successful synthesis of herbertsmithite,[4] a host of experimental techniques have been applied to study the material, including thermodynamic measurements,[1,3,5,6] neutron diffraction,[1,7] NMR,[3,8,9] and μSR.[2,3] Unfortunately, the experimental results accumulated thus far are still insufficient to determine if the material is truly a quantum spin liquid. In particular, the valence-bond solid (VBS) state proposed in Refs. 10 and 11 remains a possible alternative to the U(1) Dirac spin-liquid (DSL) state proposed in Ref. 12. In order to settle the debate of which theoretical model best describe the quantum state in herbertsmithite, further experimental probes, with guidances from theory, are probably required.

Recently, Cepas *et al.*[13] considered Raman scattering on the spin-$\frac{1}{2}$ kagome system and concluded that a generic spin-liquid state can be distinguished from a generic VBS state by the polarization dependence of the signal. They also obtained a more detailed prediction of the Raman intensity using a random-phase approximation, which may be too crude given the subtle orders[14] that may be present in the system.

In this paper, we consider the specific scenario that herbertsmithite is described by the DSL state, and make theoretical predictions of the experimental signatures that should be present in the Raman scattering. In contrast to the predictions by Cepas *et al.* (who argued that signals consist of several sharp Lorentzian peaks), we predict that *broad continua should be present in all (E_g, A_{1g}, and A_{2g}) symmetry channels*, with a superlinear power law at low energy in the A_{1g} and the E_g channels, and a linear power law in at low energy in the A_{2g} channel. In addition, we predict that *a $1/\omega$ singularity should be observed in the A_{2g} channel*. From a theoretical perspective, this $1/\omega$ singularity is particularly interesting, since it can be thought of as arising from an excitation associated with an emergent gauge boson in the system.

The paper is organized as follows: In Sec. II, the Shastry-Shraiman formulation of Raman scattering in Hubbard systems is reviewed and our disagreement with the original results by Shastry and Shraiman on the square lattice is discussed, after which the relevant results for the kagome lattice is presented (the detailed derivations and further discussions are relegated to Appendices). In Sec. III, the U(1) Dirac spin-liquid model is reviewed with important features in the mean-field theory highlighted. The Raman intensity profile in E_g channel is then presented in Sec. IV and the analogous results for the A_{1g} and A_{2g} channel are presented in Secs. V and VI, respectively. Further discussions on these results are presented in Sec. VII.

II. SHASTRY-SHRAIMAN FORMULATION

Being a strongly correlated material, herbertsmithite can be described using a one-band Hubbard model

$$H_{\mathrm{Hb}} = H_t + H_U = -\sum_{ij,\sigma} t_{ij} c_{i\sigma}^\dagger c_{j\sigma} + U \sum_i n_{i\uparrow} n_{i\downarrow}, \qquad (1)$$

where i, j label lattice sites and $\sigma = \uparrow, \downarrow$ labels spin. $c_i^\dagger$ (c_i) is the electron creation (annihilation) operator on site i and $n_{i\sigma} = c_{i\sigma}^\dagger c_{i\sigma}$.

Coupling to the external electromagnetic field can be incorporated by the replacement $c_{i\sigma}^\dagger c_{j\sigma} \mapsto c_{i\sigma}^\dagger c_{j\sigma} \exp(\frac{ie}{\hbar c}\int_j^i \mathbf{A}\cdot d\mathbf{x})$. Expanding this exponential and including also the free photon Hamiltonian H_γ, the Hamiltonian now reads

$$H = H_{\mathrm{Hb}} + H_{\gamma} + H_C,$$

$$H_C = -\sum_{ij,\sigma} t_{ij} c_{i\sigma}^{\dagger} c_{j\sigma} \left\{ \frac{ie}{\hbar c} \mathbf{A}\left(\frac{\mathbf{x}_i + \mathbf{x}_j}{2} \right) \cdot (\mathbf{x}_i - \mathbf{x}_j) - \frac{e^2}{\hbar^2 c^2} \left[\mathbf{A}\left(\frac{\mathbf{x}_i + \mathbf{x}_j}{2} \right) \cdot (\mathbf{x}_i - \mathbf{x}_j) \right]^2 + \cdots \right\},$$

$$H_{\gamma} = \sum_{\mathbf{q}} \omega_{\mathbf{q}} a_{\mathbf{q}}^{\alpha\dagger} a_{\mathbf{q}}^{\alpha}, \tag{2}$$

where $a_{\mathbf{q}}^{\alpha\dagger}$ ($a_{\mathbf{q}}^{\alpha}$) denotes the photon creation (annihilation) operator at momentum $\mathbf{q}$ and polarization α, and $\mathbf{A}(\mathbf{x})$ denotes the photon operator in real space. The $\cdots$ are terms at higher order in $\mathbf{A}$.

By treating H_C as a time-dependent perturbation, the transition rate from an initial state $|i\rangle$ to a final state $|f\rangle$ is given by

$$\Gamma_{fi} = 2\pi |\langle f|T|i\rangle|^2 \delta(\mathcal{E}_f - \mathcal{E}_i), \tag{3}$$

where $\mathcal{E}_i$ ($\mathcal{E}_f$) is the energy of the initial (final) state and $T = H_C + H_C(\mathcal{E}_i - H_{\mathrm{Hb}} - H_{\gamma} + i\eta)^{-1} H_C + \cdots$ is the T matrix.

Since the fine-structure constant $e^2/\hbar c \approx 1/137$ is small and since we are interested in Raman processes (one photon in, one photon out), only terms second order in $\mathbf{A}$ need to be retained. At this order, the T matrix reads

$$T = H_C^{(2)} + H_C^{(1)} \frac{1}{\mathcal{E}_i - (H_{\mathrm{Hb}} + H_{\gamma}) + i\eta} H_C^{(1)} = T_{\mathrm{NR}} + T_{\mathrm{R}}, \tag{4}$$

where $H_C^{(n)}$ denotes the part of H_C that is nth order in $\mathbf{A}$. The subscript R and NR on the last equality stands for resonant and nonresonant, respectively.

We are interested in a half-filled system ($\langle \Sigma_{\sigma} n_{i\sigma} \rangle = 1$) in the localized regime ($U \gg t$), in which both the initial and the final state belongs to the near-degenerate ground-state manifold $n_{i\uparrow} n_{i\downarrow} = 0$. In such case, T_{NR} has no matrix element that directly connects between the initial and the final states. Hence, only T_{R} is relevant for our purpose.

Let ω_i (ω_f), $\mathbf{k}_i$ ($\mathbf{k}_f$), and $\mathbf{e}_i$ ($\mathbf{e}_f$) be the frequency, momentum, and polarization of the incoming (outgoing) photon, respectively. Then, $\mathcal{E}_i = \omega_i + \mathcal{E}_i^{(\mathrm{Hb})} = \omega_i + \mathcal{O}(t^2/U)$, where $H_{\mathrm{Hb}}|i\rangle = \mathcal{E}_i^{(\mathrm{Hb})}|i\rangle$; and $\mathbf{A}(\mathbf{x}) \mapsto g_i \mathbf{e}_i a_{\mathbf{k}_i}^{e_i} e^{i\mathbf{k}_i \cdot \mathbf{x}} + g_f \bar{\mathbf{e}}_f a_{\mathbf{k}_f}^{e_f \dagger} e^{-i\mathbf{k}_f \cdot \mathbf{x}}$, where $g_i = \sqrt{hc^2/\omega_{\mathbf{k}_i} \Omega}$ and $g_f = \sqrt{hc^2/\omega_{\mathbf{k}_f} \Omega}$ with Ω being the appropriate volume determined by the size of the sample and/or the size of the laser spot. In much of the following we shall assume as typical that the momenta carried by the photons are much smaller than the inverse lattice spacing and hence $e^{-i\mathbf{k}_i \cdot \mathbf{x}} \approx e^{-i\mathbf{k}_f \cdot \mathbf{x}} \approx 1$. We shall also assume that the system is near resonance so that $U \gg |\omega_i - U| \gtrsim |t|$. Consequently, henceforth we shall keep only terms that are zeroth order in t/U and expand in powers of $t/(\omega_i - U)$.

Since the initial and final states both belong to the near-degenerate ground-state manifold, it should be possible to re-express T_{R} in terms of spin operators. A procedure for doing so was developed by Shastry and Shraiman.[15,16] A first step in the derivation is to expand the denominator of T_{R},

$$T_{\mathrm{R}} = H_C^{(1)} \frac{1}{\mathcal{E}_i - (H_{\mathrm{Hb}} + H_{\gamma}) + i\eta} H_C^{(1)} = H_C^{(1)} \frac{1}{\mathcal{E}_i - H_U - H_{\gamma} + i\eta} \sum_{n=0}^{\infty} \left(H_t \frac{1}{\mathcal{E}_i - H_U - H_{\gamma} + i\eta} \right)^n H_C^{(1)}. \tag{5}$$

Next, a spin quantization axis is fixed and the initial states $|i\rangle = |\{\sigma\}\rangle \otimes |\mathbf{k}_i, \mathbf{e}_i\rangle$ and final states $|f\rangle = |\{\sigma'\}\rangle \otimes |\mathbf{k}_f, \mathbf{e}_f\rangle$ are taken to be a direct product of a definite spin state in position basis with a photon energy eigenstate.[17] Then, a complete set of states is inserted in between the operators in Eq. (5). By the assumption $U \gg |\omega_i - U| \gtrsim |t|$, the intermediate states are dominated by those having no photons and exactly one holon and one doublon. Thus, they take the generic form $|r_d; r_h; \{\tau\}\rangle \otimes |\varnothing\rangle$, where $|r_d; r_h; \{\tau\}\rangle = (\Sigma_{\sigma} c_{r_d,\sigma}^{\dagger} c_{r_h,\sigma}) |\{\tau\}\rangle$ is obtained from the spin state $|\{\tau\}\rangle$ by removing an electron at r_h and putting it at r_d, and $|\varnothing\rangle$ denotes the photon vacuum state. Henceforth we shall take the abbreviation that spins are summed implicitly within pairs of electron operators enclosed by parentheses so that, e.g., $(c_i^{\dagger} c_j) = \Sigma_{\sigma} c_{i\sigma}^{\dagger} c_{j\sigma}$.

Under this insertion, $(\mathcal{E}_i - H_U - H_{\gamma})^{-1} = (\omega_i - U)^{-1}$ becomes a c number. Moreover, recall that H_t and (neglecting the photon part) H_C are sums of operators of the form $(c_i^{\dagger} c_j)$. Once a particular term is picked for each of these sums, and given an initial spin state $|\{\sigma\}\rangle$, the resulting chain of operators automatically and uniquely determines the intermediate states (which may be 0). Thus the intermediate states can be trivially resummed, and Eq. (5) becomes, in schematic form

$$\langle \{\sigma'\}|T_{\mathrm{R}}|\{\sigma\}\rangle = \sum_{i_1 j_1, i_2 j_2, \ldots} C_{i_1 j_1, i_2 j_2, \{\sigma\}} \langle \{\sigma'\}| (c_{i_2}^{\dagger} c_{j_2})(c_{i_1}^{\dagger} c_{j_1}) |\{\sigma\}\rangle + C_{i_1 j_1, \ldots, i_3 j_3, \{\sigma\}} \langle \{\sigma'\}| (c_{i_3}^{\dagger} c_{j_3})(c_{i_2}^{\dagger} c_{j_2})(c_{i_1}^{\dagger} c_{j_1}) |\{\sigma\}\rangle + \cdots. \tag{6}$$

The sum in Eq. (6) is formidable. However, if H_C and H_t connects only between sites that are a few lattice constants away, then at low order in $t/(\omega_i - U)$, except for the choice of the initial site [j_1 in Eq. (6)] the number of nonzero terms is finite and does not scale with the lattice size. Thus, Eq. (6) provides a systematic way of analyzing the contributions to the Raman intensity.

The final step in the Shastry-Shraiman formulation is to convert the chain of electron operators $(c_{i_n}^{\dagger} c_{j_n}) \cdots (c_{i_1}^{\dagger} c_{j_1})$ into spin operators using the anticommutation relation and the following spin identities

$$c_{\sigma}^{\dagger} c_{\sigma'} = \tilde{\chi}_{\sigma'\sigma} = \frac{1}{2} \delta_{\sigma',\sigma} + \mathbf{S} \cdot \boldsymbol{\tau}_{\sigma'\sigma},$$

$$c_{\sigma} c_{\sigma'}^{\dagger} = \chi_{\sigma\sigma'} = \frac{1}{2} \delta_{\sigma,\sigma'} - \mathbf{S} \cdot \boldsymbol{\tau}_{\sigma\sigma'}, \tag{7}$$

where $\mathbf{S} = c_{\sigma}^{\dagger} (\boldsymbol{\tau}_{\sigma\sigma'}/2) c_{\sigma'}$ is the spin operator for spin $\frac{1}{2}$ and τ is the usual Pauli matrices.

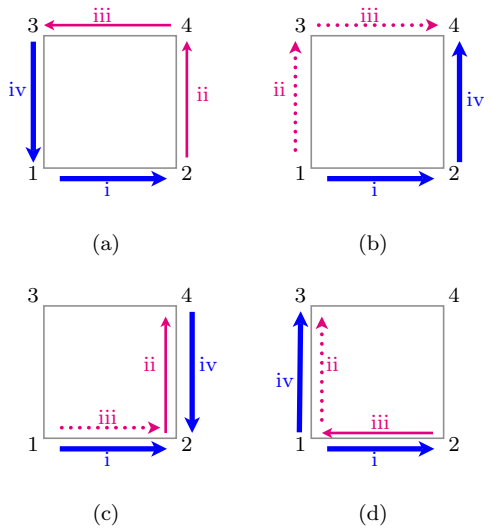

FIG. 1. (Color online) Pathways that contribute to the spin-chirality term in the square lattice. A thick (blue) arrow indicates the initial or final hop, which arises from H_C. A thin (magenta) unbroken arrow indicates the movement of a doublon, and a thin (magenta) broken arrow indicates the movement of a holon, both arising from H_t.

To the lowest nonvanishing order in $t/(\omega_i - U)$, the Shastry-Shraiman formulation reproduces the Fleury-London Hamiltonian,[18] i.e.,

$$\langle f|T_R|i\rangle = \langle\{\sigma'\}|H_{FL}|\{\sigma\}\rangle + \mathcal{O}\left[\frac{t^3}{(\omega_i - U)^2}\right],$$

$$H_{FL} = \sum_{\mathbf{r},\mathbf{r}'} \frac{2t_{\mathbf{r}\mathbf{r}'}^2}{U-\omega_i}(\mathbf{e}_i\cdot\boldsymbol{\mu})(\bar{\mathbf{e}}_f\cdot\boldsymbol{\mu})\left(\frac{1}{4} - \mathbf{S}_{\mathbf{r}}\cdot\mathbf{S}_{\mathbf{r}'}\right), \quad (8)$$

where $\boldsymbol{\mu}=\mathbf{r}'-\mathbf{r}$ is the vector that connects lattice site $\mathbf{r}$ to lattice site $\mathbf{r}'$.

For the square lattice with only nearest-neighbor hopping, *Shastry and Shraiman claimed that spin-chirality term* $\mathbf{S}_i\cdot(\mathbf{S}_j\times\mathbf{S}_k)$ *appears in the* $\bar{e}_f^x e_i^y - \bar{e}_f^y e_i^x$ *channel at the* $t^4/(\omega_i - U)^3$ *order. However, our rederivation does not confirm this result and instead concludes that the spin-chirality term vanishes to this order*. For details about our rederivation, see Appendix A. While it is hard to pin down the source of this discrepancy, two possibilities are plausible. First, the pathways that contribute to the spin-chirality term includes not only those in which a doublon or holon hops through a loop [Figs. 1(a) and 1(b)] but also those in which a holon "chases" a doublon or vice versa without involving a fourth site [Figs. 1(c) and 1(d)]. These chasing pathways are nonintuitive and could be easily missed. Second, observe that for $c_\sigma^\dagger c_{\sigma'}$, the spin indices are flipped in Eq. (7) when going from electron operators to spin operators. This, together with the applications of the anticommutation relation, can easily produce minus sign errors.

Our conclusion that the spin-chirality term vanishes to the $t^4/(\omega_i - U)^3$ order in the one-band Hubbard model need not contradict with the experimental claim that the spin-chirality term has been observed in the cuprates,[19] for in the cuprates—with the holon being delocalized as Zhang-Rice singlet while the doublon being localized at the copper site—the holon and doublon hopping magnitude need not be equal. In that case, the crucial cancellation between the four pathways in Fig. 1 no longer occurs. Furthermore, in the Shastry-Shraiman formalism the spin-chirality term may also be present at higher order in $t/(\omega_i - U)$ and/or when further neighbor hoppings are included. Since the ratio $t/(\omega_i - U)$ need not be small near resonance, these higher-order effects can manifest in experiments.

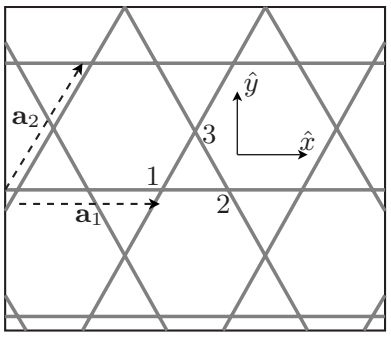

FIG. 2. The kagome lattice in real space, with the unit vectors $\hat{x}$, $\hat{y}$, primitive lattice vectors $\mathbf{a}_1$, $\mathbf{a}_2$, and lattice basis 1, 2, 3 defined.

Now we specialize to the kagome lattice and for simplicity assume that the hopping is between nearest neighbors only. Our convention of lattice basis, primitive lattice vectors, and axis alignment is shown in Fig. 2. *In contrast to the square lattice, we found a nonvanishing spin-chirality term at the* $t^4/(\omega_i - U)^3$ *order*. The contrasting result between the kagome lattice and the square lattice can be traced back to the lack of four-site loop in the former.

For theoretical calculations, it is convenient to decompose the polarization dependence of the Raman intensity into the irreducible representations (irreps) of the lattice point group, since operators belonging to different irreps do not interfere with each other (note however that subtractions between various experimental setups are often required to extract the signal that corresponds to a particular channel[16]). It is known[20] that herbertsmithite belongs to the space group $R\bar{3}m$ and hence to the point group D_{3d}. In D_{3d}, the polarization tensor $\Sigma_{\alpha,\beta=x,y}C_{\alpha,\beta}\bar{e}_f^\alpha e_i^\beta$ in the kagome plane decomposes into two one-dimensional irreps A_{1g} and A_{2g}, and one two-dimensional irrep E_g,

$$A_{1g}: \bar{e}_f^x e_i^x + \bar{e}_f^y e_i^y,$$

$$A_{2g}: \bar{e}_f^x e_i^y - \bar{e}_f^y e_i^x,$$

$$E_g \begin{cases} E_g^{(1)} : \bar{e}_f^x e_i^x - \bar{e}_f^y e_i^y \\ E_g^{(2)} : \bar{e}_f^x e_i^y + \bar{e}_f^y e_i^x \end{cases}. \quad (9)$$

To the lowest nonvanishing order in $t/(\omega_i - U)$, the A_{1g} and the E_g component of the T matrix are derived from the Fleury-London Hamiltonian (8). However, the resulting expression for the A_{1g} channel is the sum of a constant and a term proportional to the Heisenberg Hamiltonian and thus at zeroth order in t/U does not induce any inelastic transitions.

For inelastic transitions in the A_{1g} channel, the leading-order contribution appears at the $t^4/(\omega_i - U)^3$ order instead. The leading-order contribution to the A_{2g} channel also appears at the $t^4/(\omega_i - U)^3$ order. Explicitly, to leading order and neglecting the elastic part, the operators that corresponds to the different channels are

$$O_{E_g^{(1)}} = \frac{4t^2}{\omega_i - U}\sum_R \left[\frac{1}{4}\mathbf{S}_{R,3}\cdot(\mathbf{S}_{R,1}+\mathbf{S}_{R+\mathbf{a}_2,1}+\mathbf{S}_{R,2}+\mathbf{S}_{R+\mathbf{a}_2-\mathbf{a}_1,2}) - \frac{1}{2}\mathbf{S}_{R,2}\cdot(\mathbf{S}_{R,1}+\mathbf{S}_{R+\mathbf{a}_1,1})\right], \tag{10}$$

$$O_{E_g^{(2)}} = \frac{4t^2}{\omega_i - U}\sum_R \frac{\sqrt{3}}{4}[\mathbf{S}_{R,3}\cdot(\mathbf{S}_{R,1}+\mathbf{S}_{R+\mathbf{a}_2,1}) - \mathbf{S}_{R,3}\cdot(\mathbf{S}_{R,2}+\mathbf{S}_{R+\mathbf{a}_2-\mathbf{a}_1,2})], \tag{11}$$

$$\begin{aligned} O_{A_{1g}} = \frac{-t^4}{(\omega_i - U)^3}\sum_R & 2[\mathbf{S}_{R,1}\cdot(\mathbf{S}_{R+\mathbf{a}_1,1}+\mathbf{S}_{R+\mathbf{a}_2,1})+\mathbf{S}_{R,2}\cdot(\mathbf{S}_{R-\mathbf{a}_1,2} \\ & +\mathbf{S}_{R+\mathbf{a}_2-\mathbf{a}_1,2})+\mathbf{S}_{R,3}\cdot(\mathbf{S}_{R-\mathbf{a}_2,3}+\mathbf{S}_{R-\mathbf{a}_2+\mathbf{a}_1,3})] \\ & +[\mathbf{S}_{R,1}\cdot(\mathbf{S}_{R+\mathbf{a}_2-\mathbf{a}_1,2}+\mathbf{S}_{R+\mathbf{a}_1-\mathbf{a}_2,3})+\mathbf{S}_{R,2}\cdot(\mathbf{S}_{R-\mathbf{a}_2,3} \\ & +\mathbf{S}_{R+\mathbf{a}_2,1})+\mathbf{S}_{R,3}\cdot(\mathbf{S}_{R+\mathbf{a}_1,1}+\mathbf{S}_{R-\mathbf{a}_1,2})], \end{aligned} \tag{12}$$

$$\begin{aligned} O_{A_{2g}} = & \frac{2\sqrt{3}it^4}{(\omega_i - U)^3}\sum_R \Big(3\mathcal{S}_{R,1;R,2;R,3}+3\mathcal{S}_{R,1;R-\mathbf{a}_1,2;R-\mathbf{a}_2,3} \\ & +\mathcal{S}_{R,1;R,3;R+\mathbf{a}_2-\mathbf{a}_1,2}+\mathcal{S}_{R+\mathbf{a}_2,1;R,3;R,2} \\ & +\mathcal{S}_{R,3;R,2;R+\mathbf{a}_1,1}+\mathcal{S}_{R-\mathbf{a}_2+\mathbf{a}_1,3;R,2;R,1} \\ & +\mathcal{S}_{R,2;R,1;R-\mathbf{a}_2,3}+\mathcal{S}_{R-\mathbf{a}_1,2;R,1;R,3}\Big) \\ = & \frac{2\sqrt{3}it^4}{(\omega_i - U)^3}\sum_R \Big(3 \; \triangle + 3 \; \triangle + \; \square + \; \square \\ & + \; \square + \; \square + \; \square + \; \square\Big) \end{aligned} \tag{13}$$

where $\mathcal{S}_{i;;k}$ denotes $\mathbf{S}_i\cdot(\mathbf{S}_j\times\mathbf{S}_k)$. Further discussion on the derivation of these expressions can be found in Appendices.

III. U(1) DIRAC SPIN-LIQUID STATE

At half filling ($\langle\Sigma_\sigma n_{i\sigma}\rangle=1$), on the near-degenerate ground-state manifold and to the leading order in t/U, the Hubbard model is reduced to the Heisenberg model,

$$H_{\mathrm{Hsb}} = \frac{1}{2}\sum_{ij} J_{ij}\left(\mathbf{S}_i\cdot\mathbf{S}_j - \frac{1}{4}\right), \tag{14}$$

where $J_{ij}=4t_{ij}^2/U$. As in the previous section, we shall specialize to the case where the hopping is between nearest neighbor only, and hence $J_{ij}=0$ unless i, j are nearest neighbor.

In a spin-liquid state $\langle\mathbf{S}_i\rangle=0$. Thus, new variables are needed to describe the order of the system. A common choice is to introduce fermionic spinon operators $f_{i\sigma}$, $f_{i\sigma}^\dagger$ to decompose the spin operator $\mathbf{S}_i$ as follows:

$$\mathbf{S}_i = \frac{1}{2}\sum_{\alpha,\beta} f_{i\alpha}^\dagger \boldsymbol{\tau}_{\alpha,\beta} f_{i\beta}. \tag{15}$$

The occupation constraint $\Sigma_\sigma n_{i\sigma}=1$ resulting from the $U\to\infty$ limit then becomes the constraint $\Sigma_\sigma f_{i\sigma}^\dagger f_{i\sigma}=1$ on the spinons.[21,22]

Under this transformation, the spin-spin interaction $\mathbf{S}_i\cdot\mathbf{S}_j$ is mapped to a four-fermion interaction, which can be decoupled using a Hubbard-Stratonovich transformation. This yields the partition function $Z=\int DfDf^\dagger D\lambda D\chi\,\exp(-\int_0^\beta d\tau L)$, with the Lagrangian L given by

$$L = J\sum_{\langle ij\rangle}\left[|\chi_{ij}|^2 - \sum_\sigma (\chi_{ij}^* f_{i\sigma}^\dagger f_{j\sigma}+\mathrm{c.c.})\right] + \sum_{i\sigma} f_{i\sigma}^\dagger(\partial_\tau - i\lambda_i)f_{i\sigma}. \tag{16}$$

Mean-field ansatzs can be specified by treating χ_{ij} as an order parameter. Since a spin-liquid state is invariant under translation and rotation, $|\chi_{ij}|$ must be independent of i, j. Letting $\chi_{ij}=\chi e^{-ia_{ij}}$ and rewriting $\lambda_i=a_0^i$, the Lagrangian, Eq. (16), yields the following mean-field Hamiltonian,

$$H_{\mathrm{MF}} = \sum_{i\sigma} f_{i\sigma}^\dagger(ia_0^i - \mu_F)f_{i\sigma} - \chi J\sum_{\langle ij\rangle,\sigma}(e^{ia_{ij}}f_{i\sigma}^\dagger f_{j\sigma}+\mathrm{H.c.}). \tag{17}$$

Observe that an internal gauge field a^μ emerges naturally from this formulation. Its space components a_{ij} arise from the phases of χ_{ij} while its time component a_0 arises from enforcing the occupation constraint.

By gauge invariance, a mean-field ansatz for a^μ is uniquely specified by the amount of fluxes through the triangles and the hexagons of the kagome lattice. In particular, the DSL state is characterized by zero flux through the triangles and π flux through the hexagons.[10,12,14] By picking an appropriate gauge, the DSL state can be described by a tight-binding Hamiltonian with effective hopping $\tilde{t}=\pm\chi J$ on each bond. For the precise pattern of the $\pm$ signs see Fig. 3(a). Note that the unit cell for this effective tight-binding Hamiltonian is necessarily doubled as the flux enclosed by the original unit cell is π.

It is easy to check that, in units where $\chi J=1$, this effective tight-binding Hamiltonian produces the following bands,

$$E_{\mathrm{top}} = 2 \quad \text{(doubly degenerate)}, \tag{18}$$

$$E_{\pm,\mp} = -1 \pm \sqrt{3 \mp \sqrt{2}\sqrt{3-\cos 2k_x + 2\cos k_x \cos\sqrt{3}k_y}}. \tag{19}$$

At any $\mathbf{k}$ point, $E_{-,+}\le E_{-,-}\le E_{+,-}\le E_{+,+}<E_{\mathrm{top}}$. For plots of this band structure, see Fig. 4.

At low energy, the spinon spectrum is well-described by four (two spins times two $\mathbf{k}$ points) Dirac nodes, located at momentum $\pm\mathbf{Q}=\pm\pi/\sqrt{3}\hat{y}$ [cf. Figs. 3(b) and 4(a)]. More specifically, at low energy we may replace the mean-field Hamiltonian (17) by the Dirac Hamiltonian,

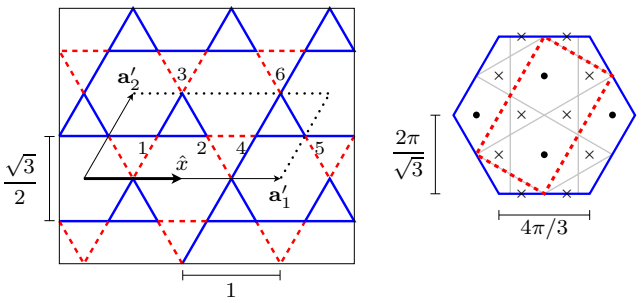

FIG. 3. (Color online) (a) The kagome lattice with the DSL ansatz. The (red) dashed lines correspond to bonds with effective hopping $\tilde{t}=-\chi J$ while (blue) unbroken lines correspond to bonds with effective hopping $\tilde{t}=\chi J$. $\mathbf{a}_1'$ and $\mathbf{a}_2'$ are the primitive vectors of the doubled unit cell. (b) The original Brillouin zone (bounded by unbroken lines) and the reduced Brillouin zone (bounded by broken lines) of the DSL ansatz. The dots indicate locations of the Dirac nodes at half filling, the crosses indicate locations of the Dirac nodes crossing the second and the third band, and the thin (gray) lines indicate saddle regions at which the band energies are the same as that at $\mathbf{k}=0$.

$$H_{\text{Dirac}} = \nu_F \sum_{\sigma,\alpha,\mathbf{q}} \psi^\dagger_{\sigma,\alpha,\mathbf{q}}(q_x\tau_x + q_y\tau_y)\psi_{\sigma,\alpha,\mathbf{q}}, \tag{20}$$

where $\sigma=\uparrow,\downarrow$ index spins, $\alpha=\pm$ index the location of the Dirac node, and $\mathbf{q}$ denotes the momentum as measured from the Dirac node. The relation between the two-component fermionic operators $\psi,\psi^\dagger$ and the spinon operators $f,f^\dagger$ defined on the lattice sites can be found in Ref. 14.

As will be explained in details below, the Dirac structure of this low-energy Hamiltonian bears important consequences for the Raman intensity at low energy. In particular, *the power-law behavior of the Raman intensity at low energy is largely resulted from the strong phase space restriction of the Dirac node structure.*

Under the DSL ansatz, we may take $|i\rangle=|i^{(\text{Hb})}\rangle\otimes|\mathbf{k}_i,\mathbf{e}_i\rangle$ and $|f\rangle=|f^{(\text{Hb})}\rangle\otimes|\mathbf{k}_f,\mathbf{e}_f\rangle$ in the transition rate, Eq. (3), where $|i^{(\text{Hb})}\rangle$ and $|f^{(\text{Hb})}\rangle$ are states obtained from filling the spinon bands. In particular, at zero temperature (which will be assumed henceforth), $|i^{(\text{Hb})}\rangle$ is simply a state with spinons filled up to the Dirac nodes at the top of $E_{+,-}$, and $|f^{(\text{Hb})}\rangle$ are states with a few spinon-antispinon pairs excited from $|i^{(\text{Hb})}\rangle$.

Moreover, the spin operators that appear in Eqs. (10)–(13) can be converted to spinon operators using Eq. (15). Explicitly,

$$\mathbf{S}_i\cdot\mathbf{S}_j = \frac{1}{4} - \frac{1}{2}f^\dagger_{i\sigma}f_{j\alpha}f^\dagger_{j\sigma'}f_{i\sigma'}, \tag{21}$$

$$\mathbf{S}_i\cdot(\mathbf{S}_j\times\mathbf{S}_k) = \frac{i}{4}[(f^\dagger_i f_j)(f^\dagger_j f_k)(f^\dagger_k f_i) - \text{H.c.}], \tag{22}$$

which allows the matrix elements between $|i^{(\text{Hb})}\rangle$ and $|f^{(\text{Hb})}\rangle$ to be calculated at mean field using Wick's theorem.

At zero temperature, to obtain the overall Raman intensity I_α for channel α at a given Raman shift $\Delta\omega=\omega_i-\omega_f$, all final states that satisfies the energy constraint $\mathcal{E}_f^{(\text{Hb})}-\mathcal{E}_i^{(\text{Hb})}=\Delta\omega$ must be summed over. Strictly enforcing this constraint is difficult in a numerical computation. Instead, we sample the final states $|f^{(\text{Hb})}\rangle$ without imposing the energy constraint but sort them into bins of energy. The overall intensity is then obtained by summing all states whose energy fall within the same bin. We perform the summation numerically using a simple Monte Carlo sampling of the momenta and band indices of the spinon and antispinon excitations in $|f^{(\text{Hb})}\rangle$.

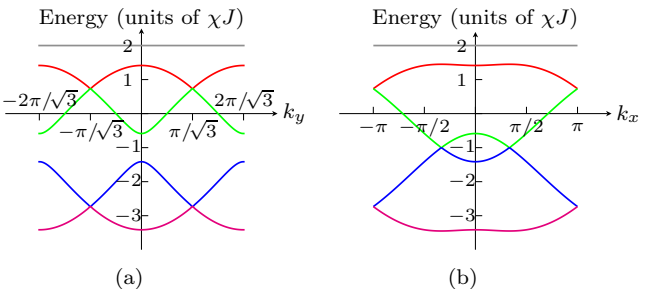

FIG. 4. (Color online) The band structure of the kagome lattice with the DSL ansatz plotted along (a) $k_x=0$ and (b) $k_y=0$. Note that the top band is twofold degenerate.

Some calculations are also performed in a slightly different way, by first converting the summed squared amplitude into a correlation function,

$$I_\alpha(\Delta\omega) = \sum_f |\langle f^{(\text{Hb})}|O_\alpha|i^{(\text{Hb})}\rangle|^2\delta(\mathcal{E}_f^{(\text{Hb})}-\mathcal{E}_i^{(\text{Hb})}-\Delta\omega)$$
$$= \int dt e^{i\Delta\omega t}\langle i^{(\text{Hb})}|O_\alpha(t)O_\alpha(0)|i^{(\text{Hb})}\rangle. \tag{23}$$

To calculate this correlation function, the spinon operators that appears in O_α [cf. Eqs. (10)–(13)] are converted from real space to momentum space, which introduces sums over momenta and band indices. Such sums are again computed by simple Monte Carlo samplings in the manner explained above. To simplify notations, in the following we shall abuse notation and write $|i\rangle$ in place of $|i^{(\text{Hb})}\rangle$ and similarly write $|f\rangle$ for $|f^{(\text{Hb})}\rangle$ whenever the context is clear.

IV. E_g CHANNEL

First consider the Raman intensity in the E_g channel, $I_{E_g}\equiv I_{E_g^{(1)}}+I_{E_g^{(2)}}$. By computing the correlation function, Eq. (23) (with $\alpha=E_g^{(1)}$ and $E_g^{(2)}$), we obtain the Raman intensity profile as shown in Fig. 5.

From Fig. 5, it can be seen that the Raman response take the form of a broad continuum ranging from approximately $1.5\chi J$ to approximately $11\chi J$, with occasional sharp spikes. The existence of a continuum is not a surprise, since the operators $O_{E_g^{(1)}}$ and $O_{E_g^{(2)}}$ in Eqs (10) and (11) corresponds to two-spinon two-antispinon operators in the DSL ansatz, and hence the final states $|f\rangle$ are spinon-antispinon pairs and thus there is a continuum of phase space for excitations. The cutoff near $11\chi J$ is also natural, since the total bandwidth in the DSL ansatz is approximately $6\chi J$, and hence with two spinons and two antispinons the excitation energy is at most $12\chi J$. The sharp peaks and the low-energy suppression, however, require further investigations.

To gain more insight into how the various features in Fig. 5 comes about, it is useful to consider the sum over final states explicitly. Given the form of $O_{E_g^{(1)}}$ and $O_{E_g^{(2)}}$ in Eqs. (10) and (11), there are two types of final states: the first consists of two spinon-antispinon pairs excited from the ground state $|i\rangle$ while the second consists of *one* spinon-antispinon pair excited from $|i\rangle$. Schematically, these take the form

$$|f_{2\text{ pairs}}\rangle = f^\dagger_{k_1,n_1,\sigma} f_{k_2,n_2,\sigma} f^\dagger_{k_3,n_3,\sigma'} f_{k_4,n_4,\sigma'} |i\rangle, \tag{24}$$

$$|f_{1\text{ pair}}\rangle = f^\dagger_{k_1,n_1,\sigma} f_{k_2,n_2,\sigma} |i\rangle. \tag{25}$$

In both cases the momentum conservation $\Sigma_{i\text{ odd}}\mathbf{k}_i = \Sigma_{i\text{ even}}\mathbf{k}_i$ holds, and that the band index n_i denotes one of the top three (empty) bands when i is odd and one of the bottom three (occupied) bands when i is even.

For the one-pair final state to have a nonzero matrix element with the initial state, a pair of spinon-antispinon operator must self-contract within $O_{E_g^{(1)}}$ and $O_{E_g^{(2)}}$, e.g.,

$$\begin{aligned} f^\dagger_{i\sigma} f_{j\sigma} f^\dagger_{j\sigma'} f_{i\sigma'} \mapsto & \langle f^\dagger_{i\sigma} f_{j\sigma}\rangle f^\dagger_{j\sigma'} f_{i\sigma'} + f^\dagger_{i\sigma} f_{j\sigma} \langle f^\dagger_{j\sigma'} f_{i\sigma'}\rangle \\ & - \langle f^\dagger_{i\sigma} f_{i\sigma'}\rangle f^\dagger_{j\sigma'} f_{j\sigma} - \langle f^\dagger_{j\sigma'} f_{j\sigma}\rangle f^\dagger_{i\sigma} f_{i\sigma'} \\ = & \chi_{ij} f^\dagger_{j\sigma} f_{i\sigma} + \chi_{ji} f^\dagger_{i\sigma} f_{j\sigma} - \frac{1}{2}(f^\dagger_{i\sigma} f_{i\sigma} + f^\dagger_{j\sigma} f_{j\sigma}), \end{aligned} \tag{26}$$

where the spin indices σ, σ' are summed in the above. The mean-field parameter χ_{ij} here is the same as the one introduced in Sec. III.

However, one should be mindful that while the constraint $\Sigma_\sigma f^\dagger_{j\sigma} f_{j\sigma} = 1$ is strictly enforced in the exact spin-liquid state, it is enforced only on average in the mean-field representation. Therefore, *while operators of the form* $f^\dagger_{j\sigma} f_{j\sigma}$ *should induce no transition between* $|i\rangle$ *and* $|f\rangle$, *the matrix element* $\langle f|f^\dagger_{j\sigma} f_{j\sigma}|i\rangle$ *may be nonzero at mean field*. To avoid such problem, we shall throw away the $f^\dagger_{j\sigma} f_{j\sigma}$ terms in Eq. (26) by hand.

With this precaution, we recalculated I_{E_g} by numerically sampling the final states, and we do so for the one-pair and two-pair contributions separately. The results are shown in Figs. 6 and 7. We have verified that the sum of Raman intensities from the two figures (with the relative ratio determined by the details of the numerical calculations) produces an overall intensity profile that matches Fig. 5.

The density of states (DOS) for two-pair and one-pair excitations having zero total momenta have been plotted alongside with the respective Raman intensities in Figs. 6 and 7. From the figures, it can be seen that the DOS matches the Raman intensity profile very well for two-pair excitations and less so (but still reasonably well) for one-pair excitations. This can be understood by rewriting the first line of Eq. (23) as $I_\alpha(\Delta\omega) = \overline{|\langle f|O_\alpha|i\rangle|^2}\mathcal{D}(\Delta\omega)$ in which $\mathcal{D}(\mathcal{E})$ denotes the density of state at energy $\mathcal{E}$ and $\overline{|\langle f|O_\alpha|i\rangle|^2}$ denotes the average matrix element squared at the same energy. From this, the DOS is expected to match the Raman intensity well as long as the average matrix element does not change drastically with energy—an assumption more valid for two-pair states as opposed to one-pair ones because of the larger phase space available in the former case.

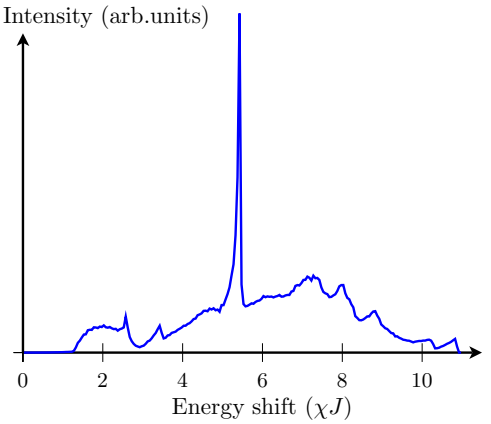

FIG. 5. (Color online) Raman intensity in the E_g channel, computed using the correlation, Eq. (23), with a bin size of $0.05\chi J$ in energy.

Moreover, the sharp peak appearing near $5.5\chi J$ in Fig. 5 can now be attributed to one-pair excitations, which can in turn be attributed to a peak in the one-pair DOS. From the band structure (Fig. 4), it can be checked that $\Delta\omega = 5.41\chi J$ *corresponds to the energy difference between the top flat band and the saddle point* $\mathbf{k}=\mathbf{0}$ *at the bottom band*. The enhanced phase space near this energy is thus the likely cause of this peaklike feature.

Next, we consider the low-energy ($\Delta\omega < 2\chi J$) part the of Raman intensity more carefully, checking if the intensity profile is an exponential or a power law, and determining the exponent if the latter case holds. To enhance the quality of the data, and since only the low-energy behavior concerns us, we resample the final states, restricting the antispinon to the highest-occupied band $E_{+,-}$ and the spinon to the lowest-

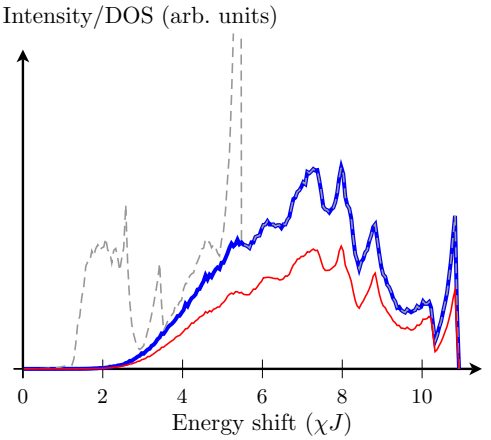

FIG. 6. (Color online) Plots of density of states (thin red curve) and E_g Raman intensity (thick blue curve) contributed by final states having two spinon-antispinon pairs, together with the overall E_g Raman intensity (broken gray curve), all computed with a bin size of $0.05\chi J$ in energy. Note that the relative scale between the intensity plots and the DOS plot is arbitrary and is set here such that both curves are visible.

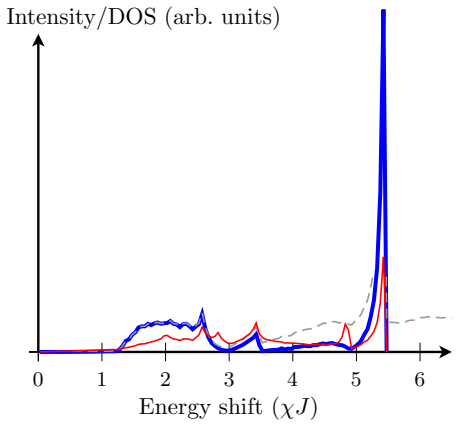

FIG. 7. (Color online) Plots of density of states (thin red curve) and E_g Raman intensity (thick blue curve) contributed by final states having one spinon-antispinon pair, together with the overall E_g Raman intensity (broken gray curve), all computed with a bin size of $0.05\chi J$ in energy. Note that the relative scale between the intensity plots and the DOS plot is arbitrary.

unoccupied band $E_{+,+}$ (despite this, the two-pair data is consistently nonzero only above $\Delta\omega=0.4\chi J$). The resulting data are shown in the log-log plots in Figs. 8 and 9. Since the smaller exponent dominates as $\Delta\omega\to 0$, the *overall Raman intensity in the E_g channel scales roughly as $I_{E_g}\propto(\Delta\omega)^3$ at low energy*.

From the plots, it is clear that the DOS and the Raman intensity both follow a power law with a higher exponent for the two-pair excitations as compared to the one-pair ones. *Analytically, it is easy to check that $\mathcal{D}_{1\text{ pair}}\propto\Delta\omega$ for the Dirac Hamiltonian* (20), since the integral involves four components of momenta subjected to three constraints (energy and momentum conservation), and that $|\mathbf{q}|$ scales as energy. *Similarly, it is easy to check that $\mathcal{D}_{2\text{ pair}}\propto(\Delta\omega)^5$ in the Dirac Hamiltonian*. Furthermore, since the eigenstates of the Dirac Hamiltonian depend only on $\theta=\tan^{-1}(q_y/q_x)$ but not on $|\mathbf{q}|$, *the average matrix element squared $|\langle f|O_\alpha|i\rangle|^2$ must be constant in energy*. However, to the $t^2/(\omega_i-U)$ order in the E_g channel [Eqs. (10) and (11)], the matrix element turns out to be exactly zero for all one-pair excitations in the Dirac

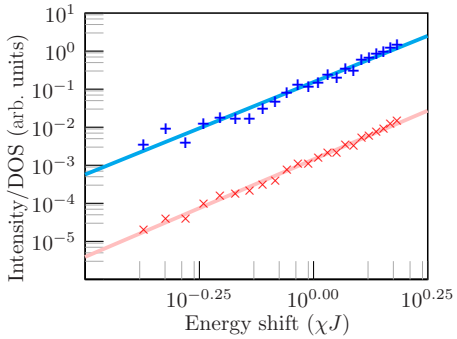

FIG. 8. (Color online) Log-log plot of the DOS (red × symbols) and Raman intensity in the E_g channel (blue + symbols) for two-pair excitations. Simple linear fits (straight lines in pink and cyan) give a slope of 5.1 for the DOS data and 4.9 for the Raman intensity data.

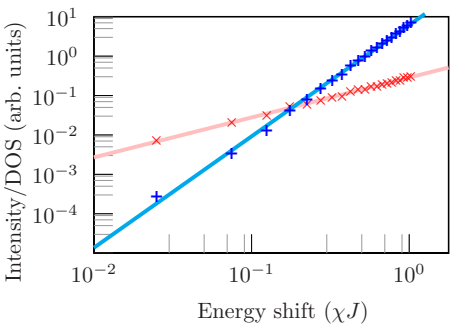

FIG. 9. (Color online) Log-log plot of the DOS (red × symbols) and Raman intensity in the E_g channel (blue + symbols) for one-pair excitations. Simple linear fits (straight lines in pink and cyan) give a slope of 1.0 for the DOS data and 2.8 for the Raman intensity data.

Hamiltonian. Hence, at low energy, we expect $I_{2\text{ pair}}\propto\mathcal{D}_{2\text{ pair}}\propto(\Delta\omega)^5$ and $I_{1\text{ pair}}\propto(\Delta\omega)^\alpha$ with $\alpha>1$, consistent with the numerical results in Figs. 8 and 9.

Since $\mathcal{D}_{1\text{ pair}}\propto\Delta\omega$, it leaves open the possibility that $I_{E_g}\propto\Delta\omega$ at higher order in $t/(\omega_i-U)$. While we are not able to rule out this possibility, we do find that *the vanishing of matrix elements in the Dirac Hamiltonian for all one-pair excitations persist to the $t^4/(\omega_i-U)^3$ order* (the derivation of O_{E_g} to this order can be found in Appendix B).[23] Hence, even if $I_{E_g}\propto\Delta\omega$ at some higher order, its effect will not be prominent unless the system is sufficiently near resonance.

In the data presented above we have summed the contributions arising from $O_{E_g^{(1)}}$ and $O_{E_g^{(2)}}$. By computing the two contributions separately, it can be checked that each contribute equally. In fact, we have checked that *the intensity profiles are essentially identical upon an arbitrary rotation in the kagome plane for the one-pair and two-pair excitations separately*. In other words, we found that the quantity $I_{E_g}(\Delta\omega,\theta)$, defined by

$$I_{E_g}(\Delta\omega,\theta)=\sum_f|\langle f|O_{E_g^{(1)}}\cos\theta+O_{E_g^{(2)}}\sin\theta|i\rangle|^2\times\delta(\mathcal{E}_f^{(\mathrm{Hb})}-\mathcal{E}_i^{(\mathrm{Hb})}-\Delta\omega),\tag{27}$$

is independent of θ, and remain so even if the sum is restricted to one-pair or two-pair states. Our numerical results are thus consistent with the analytical arguments given by Cepas *et al.*[13]

V. A_{1g} CHANNEL

Using $O_{A_{1g}}$ in Eq. (12) in place of $O_{E_g^{(1)}}$ and $O_{E_g^{(2)}}$, we repeat the calculation of the Raman intensity profile for the A_{1g} channel. The results are shown in Fig. 10. From the figure, we see that the Raman intensity profile of the A_{1g} channel also has a broad continuum up to a cutoff near $11\chi J$. However, the sharp peak near $5.5\chi J$ that appears in the E_g channel is markedly missing.

Decomposing the Raman intensity into one-pair and two-pair contributions as in Sec. IV, we see that *the overall Raman intensity profile in the A_{1g} channel is dominated by the*

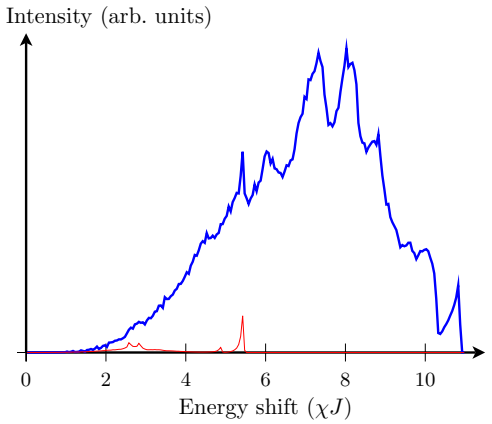

FIG. 10. (Color online) Plots of the overall Raman intensity (thick and blue) and its contribution by one-pair states (thin and red) in the A_{1g} channel, both with the same vertical scale and computed with a bin size of $0.05\chi J$ in energy.

two-pair states. Since the sharp peak near $5.5\chi J$ is originated from the one-pair contribution, this explains the absence of sharp peak in the A_{1g} channel.

However, at low energy ($\Delta\omega \lesssim 1.5\chi J$) the Raman intensity profile is still dominated by the one-pair contribution. And by plotting the Raman intensity profile in a log-log scale (Fig. 11), we see that the low-energy behavior is characterized by a power law with exponent $\alpha \approx 3$, similar to the value obtained in the E_g channel. Again, it can be checked on analytical ground[23] that the matrix element vanishes for all one-pair state in the Dirac Hamiltonian, consistent with the numerical results.

VI. A_{2g} CHANNEL

For the A_{2g} channel, to the leading order in $t/(\omega_i - U)$, the Raman process receives contributions from excited states having one, two, and three pairs of spinon antispinon. The overall Raman intensity coming from these spinon-antispinon pairs are plotted in Fig. 12. It can be seen that the continuum also appears in this channel, now ranging from $0\chi J$ up to approximately $16\chi J$, which corresponds to approximately three times the total spinon bandwidth. Moreover, sharp peaks not unlike the one in the E_g channel are

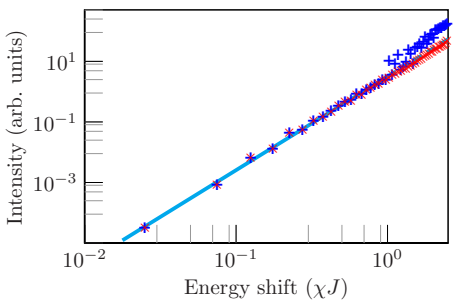

FIG. 11. (Color online) Log-log plot of the Raman intensity (blue + symbols) and its contribution by one-pair states (red × symbols) in the A_{1g} channel. Simple linear fit (straight line in cyan) for the one-pair data up to $\Delta\omega = \chi J$ gives a slope of 3.1.

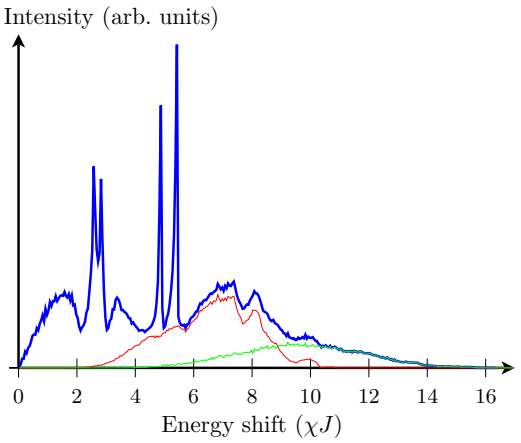

FIG. 12. (Color online) Raman intensity in the A_{2g} channel arising from spinon-antispinon pairs (thick and blue), and its contribution from two-pair (thin and red) and three-pair (thin and green) states. All computed with a bin size of $0.05\chi J$ in energy.

observed at various energies. Again, it can be checked that these sharp peaks can be attributed to the various features of the DSL bands, particularly to the *flat-band-to-saddle* and *saddle-to-saddle* transitions.

Note that *the low-energy Raman transition is much more prominent in the A_{2g} channel* than that in the E_g and A_{1g} channels. In particular, the Raman intensity in this channel has a broad peak near $\Delta\omega = 1.5\chi J$, below which it is visibly linear. From Fig. 12, the prominence of low-energy Raman transition trace back to the relatively large average matrix elements in the one-pair transitions. Moreover, the linear behavior suggests that $\overline{|\langle f|O_\alpha|i\rangle|^2}$ no longer vanishes in the Dirac Hamiltonian so that $I_{1\text{ pair}} \propto \mathcal{D}_{1\text{ pair}} \propto \Delta\omega$ at low energy.

The forgoing discussion neglected an important contribution to the A_{2g} Raman intensity. Recall that in computing the one-pair contribution, a mean-field factorization is performed [Eq. (26)], in which the Hubbard-Stratonovich variable χ_{ij} is treated as a constant. However, because of the emergent gauge structure in the U(1) spin-liquid theory, Eq. (17), the dynamics of the phase of χ_{ij} cannot really be neglected. Fortunately, since the projection of the T matrix onto the E_g and A_{1g} channel, Eqs. (10)–(12), involves no nontrivial closed path, the results presented above should still be *qualitatively* correctly, even though quantitative corrections to the detailed predictions (such as the exponents of the power laws at low energy) may be present.

The situation for the A_{2g} channel is different, as can be seen by considering the full contraction of the spin-chirality term $\mathbf{S}_1 \cdot (\mathbf{S}_2 \times \mathbf{S}_3)$ into χ_{ij},

$$
\begin{aligned}
i\mathbf{S}_1 \cdot (\mathbf{S}_2 \times \mathbf{S}_3) &= \frac{1}{4}[(f_1^\dagger f_3)(f_3^\dagger f_2)(f_2^\dagger f_1) - \text{H.c.}] \\
&\mapsto \frac{1}{4}(\chi_{13}^{(0)} e^{ia_{13}} \chi_{32}^{(0)} e^{ia_{32}} \chi_{21}^{(0)} e^{ia_{21}} - \text{H.c.}) + \cdots \\
&= (Ce^{i(a_{13}+a_{32}+a_{21})} - \text{H.c.}) + \cdots, \qquad (28)
\end{aligned}
$$

where $\chi_{ij}^{(0)}$ denotes the part of χ_{ij} that can be treated as con-

stant and $C=\chi_{13}^{(0)}\chi_{32}^{(0)}\chi_{21}^{(0)}/4$. For convenience we shall denote $(Ce^{i(a_{ik}+a_{kj}+a_{ji})}-\text{H.c.})$ as Q_{ijk} henceforth.

Note that $e^{i(a_{13}+a_{32}+a_{21})}$ is the emergent gauge flux enclosed by the loop $1\to3\to2\to1$. *Since the emergent gauge field is fluctuating, this gauge flux can lead to an excitation of the kagome system.* Physically, the excitations generated by Q can be thought of as a *collective* excitation in the system, which exists on top of the individual spinon-antispinon excitations. This is analogous to the situation in an ordinary Fermi liquid, where plasmon mode exists on top of the electron-hole continuum.

Since the fluctuation of a_{ij} can be considered as a collective excitation in the system, as an approximation we may consider the final states $|f_{\text{gauge}}\rangle$ connected to ground state by Q to be lying in a separate sector than the spinon-antispinon pairs previously considered. Then, the total Raman intensity in the A_{2g} channel can be obtained by adding the contributions by these collective states to the contributions by the spinon-antispinon pair states.

The contribution to the Raman intensity by $|f_{\text{gauge}}\rangle$ can be computed from the QQ correlator. To do so, we start with Eq. (28), take the continuum limit, and Taylor expand the exponential. Then, $a_{13}+a_{32}+a_{21}\mapsto\oint_{\wp_{132}}\mathbf{a}\cdot d\mathbf{x}=\int\int_{\Omega_{132}}bd^2\mathbf{x}$, where $b=\partial_x a_y-\partial_y a_x$ is the emergent "magnetic" field. Here $\wp_{132}$ denotes the closed loop $1\to3\to2\to1$ and Ω_{132} denotes the area enclosed by this path. Thus, $Q_{ijk}\approx2i|C|[\sin(\phi_0)+\cos(\phi_0)\int\int_{\Omega_{ijk}}bd^2\mathbf{x}]\approx2i|C|[\sin(\phi_0)+\cos(\phi_0)\Omega_{ijk}b(\mathbf{r}_{ijk})]$, where $C=|C|e^{i\phi_0}$ and $\mathbf{r}_{ijk}$ denotes the position of the three-site loop.[24] The QQ correlator is thus converted into a bb correlator. Hence,

$$I_{A_{2g}}^{(\text{gauge})}\approx C'\int dt e^{i\Delta\omega t}\langle i|\left[\sum_{\mathbf{R}}\sum_{\Delta's}b(\mathbf{r}_{ijk},t)e^{-i\mathbf{q}\cdot\mathbf{r}_{ijk}}\right]^{\dagger}\times\left[\sum_{\mathbf{R}}\sum_{\Delta's}b(\mathbf{r}_{ijk},0)e^{-i\mathbf{q}\cdot\mathbf{r}_{ijk}}\right]|i\rangle, \tag{29}$$

where C' is a numerical constant and will not be kept track of below. Note that the photon momentum has been restored, which introduce the factor $e^{-i\mathbf{q}\cdot\mathbf{r}_{ijk}}$, with $\mathbf{q}=\mathbf{k}_i-\mathbf{k}_f$ the momentum transferred to the lattice. The $\Sigma_{\Delta's}$ is a shorthand for summing over the different three-site geometries on a unit cell with the appropriate coefficients, as is shown in Eq. (13).

Since $b=\partial_x a_y-\partial_y a_x$, $b(\mathbf{x})=\Sigma_k(i\mathbf{k}\times\boldsymbol{\epsilon}_k)a_{\mathbf{k}}e^{i\mathbf{k}\cdot\mathbf{x}}-(i\mathbf{k}\times\boldsymbol{\epsilon}_k^*)a_{\mathbf{k}}^{\dagger}e^{-i\mathbf{k}\cdot\mathbf{x}}$, where $\boldsymbol{\epsilon}_k$ is the polarization of the emergent gauge field at momentum $\mathbf{k}$. Moreover, $a_k|i\rangle=0$ and $\langle i|a_k^{\dagger}=0$. Hence, upon Fourier transform,

$$I_{A_{2g}}^{(\text{gauge})}\propto\langle i|(i\mathbf{q}\cdot\boldsymbol{\epsilon}_q)a_{\mathbf{q}}(\Delta\omega)a_{\mathbf{q}}^{\dagger}(0)(-i\mathbf{q}\cdot\boldsymbol{\epsilon}_q^*)|i\rangle. \tag{30}$$

The correlator that we need to compute is thus one of a gauge field in 2+1 dimensions coupled to relativistic fermions [i.e., fermions described by the Dirac Hamiltonian (20)]. This situation has been considered by Ioffe and Larkin[25] under the context of high-T_c superconductivity, who found that,

$$\Pi_{\alpha\beta}(\mathbf{q},\omega_E)=\frac{1}{8}\frac{\omega_E^2\delta_{\alpha\beta}+v_F^2q^2\delta_{\alpha\beta}-v_F^2q_\alpha q_\beta}{(\omega_E^2+v_F^2q^2)^{1/2}}, \tag{31}$$

where $\Pi_{\alpha\beta}(\mathbf{q},\omega_E)$ is the polarization function of the gauge field in Euclidean space time and $v_F=\chi Ja/\sqrt{2}\hbar$ is the Fermi velocity at the Dirac node. Hence,

$$I_{A_{2g}}^{(\text{gauge})}\propto-q^2\,\text{Im}\left\{\frac{8}{(v_F^2q^2-\Delta\omega^2+i\eta)^{1/2}}\right\}+\cdots\propto\frac{q^2\Theta(\Delta\omega-v_Fq)}{(\Delta\omega^2-v_F^2q^2)^{1/2}}+\cdots. \tag{32}$$

For herbertsmithite, v_F is estimated[14] to be 5.0×10^3 m/s. Hence, even at backscattering and with optical light at wavelength $\lambda\approx500$ nm, v_Fq corresponds to a frequency shift of approximately 4.0 cm^{-1} only, which is too small to be resolved by current instruments. Therefore, the collective excitation associated with the gauge flux will appear as *a characteristic* $1/\omega$ *singularity* in experiments.

Physically, if the gauge boson is nondissipative, the Green's function would have a simple pole, corresponding to a sharp delta-function-like signal. That we have a $1/\omega$ singularity in place of a delta function tells us that the gauge photon mode is strongly dissipative and is in fact overdamped. Following the analogy with the ordinary plasmon mode as stated above, this dissipative behavior of the emergent gauge boson can be thought of as the analog of the Landau damping.

VII. DISCUSSION

In the previous sections we presented calculations of Raman intensity profile based on the Shastry-Shraiman formalism, assuming the validity of the U(1) Dirac spin-liquid state. We found a broad continuum in the Raman intensity profile in all symmetry channels, each displays a power-law behavior at low energy. Moreover, the profiles are found to be invariant under arbitrary rotations in the kagome plane. For the E_g and the A_{2g} channels, the continuum is accompanied by occasional sharp peaks that can be attributed to the various features of the DSL bands. In addition, the Raman intensity profile in the A_{2g} channel also contains a characteristic $1/\omega$ singularity, which arose in our model from an excitation of the emergent U(1) gauge field.

However, several caveats in our theoretical predictions should be noted. First, in order to compare with experimental data, χJ must be converted to physical units. In Ref. 14, Hermele *et al.* estimated χ by fitting the spectrum of projected one-particle excitations to the mean-field band structure and found that $\chi\approx0.40$. Together with $J\approx190$ K, this gives $\chi J\approx56$ cm^{-1}. However, there is considerable uncertainty in this estimation, and so it may be a good idea to take χ as a fitting parameter when comparisons with experiments are made.

Second, when the contribution to the Raman intensity profile by spinon-antispinon pairs are calculated, the excited spinons and antispinons have essentially been treated as free fermions. However, they should really be regarded as complicated composite fermions, which interact with each other

through an effective gauge field. Consequently, the actual excitation spectrum of the quasiparticles will almost certainly look *quantitatively* different from the ones presented here. Specifically, there may be finite lifetime effects, particularly prominent at high energy, that causes the Raman intensity profile to be "washed out" compared with the ones presented here. Because of this, the sharp peaks that appear in Figs. 5 and 12 may not be present in the actual data. Furthermore, while the low-energy power-law structure of the Raman intensity profile is expected to survive, the detailed exponent is almost certainly modified from their mean-field values. Similarly, the contribution of Raman intensity in the A_{2g} channel by the emergent gauge boson may scale as $I_{A_{2g}}^{(\text{gauge})} \propto (\Delta\omega)^{\alpha}$ with α modified from -1.

Third, in our derivation of the operators that correspond to the Raman transitions in the different channels, Eqs. (10)–(13), we stopped at the zeroth order in t/U and the leading order in $t/(\omega_i - U)$. While terms higher order in t/U can be safely neglected, the same cannot be said for $t/(\omega_i - U)$, particularly near resonance ($\omega_i \approx U$). Therefore, these higher-order contributions, which modify the Raman intensity profile from those presented in the previous sections, may show up in actual data. In particular, the Raman intensity profile may not exhibit the abrupt drops as in Figs. 5 and 10. Furthermore, since $\mathcal{D}_{1\ \text{pair}} \propto \Delta\omega$, a power law with exponent much closer to 1 may be found in the E_g and A_{1g} channels at low energy.

Fourth, while we argued that a $1/\omega$ singularity should be present in the A_{2g} channel, we have lost track of the ratio between its contribution and that by the spinon-antispinon pairs. Since the intensity of this singularity is proportional $|\mathbf{q}|^2$, it may be difficult to detect in optical Raman spectroscopy, in which the momentum transfer $\mathbf{q}$ is much smaller than the inverse of lattice constant.

In Sec. I, we mentioned the VBS state as a close competitor of the DSL state, as well as the proposal by Cepas *et al.* to distinguish between the two using the angular dependence of the Raman intensity profile. In light of the results presented in this paper, there is another feature in the Raman spectrum that can be used to distinguish between the two states. For *in general, in a VBS state the spin excitations is gapped while in a spin-liquid state it is gapless. Consequently, the Raman intensity profile should show an exponential dependence in the former case and a power-law dependence in the latter case.*

Recently, Wulferding and Lemmens[26] have obtained Raman intensity data for herbertsmithite. Their data, extending from 30 to 1500 cm^{-1}, shows a broad background that persists beyond 500 cm^{-1}, in addition to a quasielastic line and several sharp peaks at finite frequency shifts. Furthermore, at low temperature (5 K) the quasielastic line is suppressed and the low-energy portion of their data shows a linear dependence with respect to the Raman shift. While their data are quantitatively different from the results of our theoretical calculations presented in Secs. IV–VI, the existence of a broad continuum can be seen as consistent with the U(1) Dirac spin-liquid model, even though the appearances of the other features would require the consideration of extra contributions (e.g., from the Zn impurities[5,20]) that are not present in our model.

ACKNOWLEDGMENTS

We thank B. S. Shastry, B. I. Shraiman, and Naoto Nagaosa for discussions on the derivation of the Raman scattering T matrix, Yi Zhou for discussions on the numerical calculations, and Peter Lemmens for discussions on his experimental data and for helpful comments on our manuscript. This research is partially supported by NSF under Grant No. DMR-0804040.

APPENDIX A: DERIVATION OF THE RAMAN TRANSITION IN THE A_{2g} channel

In this section we shall consider the derivation of Raman transition rate in the $\bar{e}_f^x e_i^y - \bar{e}_f^y e_i^x$ channel in more details. For completeness, we shall present derivations not only for the kagome lattice, but also for the square, the triangular, and the hexagonal ones. Although the irreducible representation that corresponds to the polarization $\bar{e}_f^x e_i^y - \bar{e}_f^y e_i^x$ may be named differently in these lattices, we shall abuse notation and continue to refer to them as the "A_{2g}" channel. We shall show that, contrary to claim by Shastry and Shraiman, the matrix elements in the A_{2g} channel vanishes up to the $t^4/(\omega_i - U)^3$ order in the square lattice according to their formalism.

To extract the A_{2g} channel from the general polarization matrix, note that given any particular hopping pathway, a "reversed pathway" can be constructed, in which all electron operators are conjugated and their order reversed [for example, $(c_1^\dagger c_2)(c_2^\dagger c_3)(c_3^\dagger c_1)$ is the reversed pathway of $(c_1^\dagger c_3)(c_3^\dagger c_2)(c_2^\dagger c_1)$]. Then, $\bar{e}_f^x e_i^y \mapsto \bar{e}_f^y e_i^x$ and the order the spin operators thus obtained are inverted. Hence, to the $t^4/(\omega_i - U)^3$ order, which corresponds to at most four spin operators, the only terms that survive in the A_{2g} channel are the spin-chirality operators $\mathbf{S}_i \cdot (\mathbf{S}_j \times \mathbf{S}_k)$. Thus, in our derivation it suffices to extract the spin-chirality contributions from pathways whose initial and final currents are not colinear.

To depict the hopping pathways efficiently, the following abbreviations are introduced in the diagrams, with colors referring to the online edition. A thick (blue) arrow is used to indicate the initial or the final hop in which a holon-doublon pair is created or destroyed. For the internal hops, the movement of a doublon is indicated by a thin (magenta) unbroken arrow and the movement of a holon is indicated by a thin (magenta) broken arrow. Lower case roman letters are used to indicate the ordering of hops. Note that in this scheme, an unbroken magenta arrow from i to j corresponds to the electron operators $(c_j^\dagger c_i)$, while a broken magenta arrow from i to j corresponds to the electron operators $(c_i^\dagger c_j)$.

The lowest order at which the spin-chirality term can show up is $t^3/(\omega_i - U)^2$, which corresponds to pathways with one internal hop. Such pathway can be found in the triangular or the kagome lattice, or when next-nearest hopping is included. We shall show that the contributions to the A_{2g} channel by these pathways cancel in pairs at this order.

It is easy to see that there are two types one-internal-hop pathways in general, both involving three lattice sites. In a pathway of the first type, a holon-doublon pair is created across a bond by an incident photon. Then, the doublon moves to a third site before recombining with the holon to

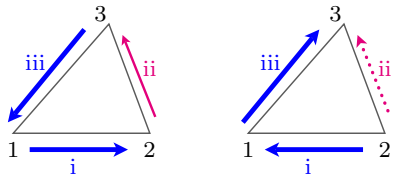

FIG. 13. (Color online) Two types of one-internal-hop pathways. Thick (blue) arrows denote initial or final hop in which a holon-doublon pair is created or destroyed, thin (magenta) unbroken arrows denote the movement of a doublon, and thin (magenta) broken arrows denote the movement of a holon. Lower case roman letters are used to indicate the order of hops. In (a) the internal hop is performed by the doublon while in (b) the internal hop is performed by the holon.

emit a Raman-shifted photon [Fig. 13(a)]. A pathway of the second type is similar, except that it is the *holon* that moves to a third site before recombining [Fig. 13(b)].

Applying the procedures as explained in Sec. II, the operator that corresponds to the pathway in Fig. 13(a) is given by

$$\begin{aligned} T_{1,e} &= (\bar{\mathbf{e}}_f \cdot \mathbf{x}_{13})(\mathbf{e}_i \cdot \mathbf{x}_{21}) \frac{(-it_{13})(-t_{32})(-it_{21})}{(\omega_i - U)^2} \\ &\quad \times (c_1^\dagger c_3)(c_3^\dagger c_2)(c_2^\dagger c_1) \\ &= (\bar{\mathbf{e}}_f \cdot \mathbf{x}_{13})(\mathbf{e}_i \cdot \mathbf{x}_{21}) \frac{t_{13}t_{32}t_{21}}{(\omega_i - U)^2} \mathrm{tr}\{\chi_3 \chi_2 \tilde{\chi}_1\} \\ &\doteq (\bar{\mathbf{e}}_f \cdot \mathbf{x}_{13})(\mathbf{e}_i \cdot \mathbf{x}_{21}) \frac{t_{13}t_{32}t_{21}}{(\omega_i - U)^2} 2i \mathbf{S}_3 \cdot \mathbf{S}_2 \times \mathbf{S}_1, \end{aligned} \quad \text{(A1)}$$

where $\mathbf{x}_{ij}=\mathbf{x}_i-\mathbf{x}_j$ is the vector from site j to site i, and "$\doteq$" denotes equality upon neglecting terms that do not contribute to the A_{2g} channel.

Similarly, the operator that corresponds to the pathway in Fig. 13(b) is given by

$$\begin{aligned} T_{1,h} &= (\bar{\mathbf{e}}_f \cdot \mathbf{x}_{31})(\mathbf{e}_i \cdot \mathbf{x}_{12}) \frac{(-it_{31})(-t_{23})(-it_{12})}{(\omega_i - U)^2} \\ &\quad \times (c_3^\dagger c_1)(c_2^\dagger c_3)(c_1^\dagger c_2) \\ &= (\bar{\mathbf{e}}_f \cdot \mathbf{x}_{31})(\mathbf{e}_i \cdot \mathbf{x}_{12}) \frac{t_{31}t_{23}t_{12}}{(\omega_i - U)^2} (-1) \mathrm{tr}\{\chi_1 \tilde{\chi}_2 \tilde{\chi}_3\} \\ &\doteq (\bar{\mathbf{e}}_f \cdot \mathbf{x}_{31})(\mathbf{e}_i \cdot \mathbf{x}_{12}) \frac{t_{31}t_{23}t_{12}}{(\omega_i - U)^2} 2i \mathbf{S}_1 \cdot \mathbf{S}_2 \times \mathbf{S}_3 \doteq -T_{1,e}, \end{aligned} \quad \text{(A2)}$$

where t_{ij} are assumed to be real in the last step.

Since the two pathways depicted in Fig. 13 always come in pair, the contribution to the A_{2g} channel by one-internal-hop pathways vanishes upon summing as claimed.

Now consider pathways that involve two internal hops, starting with the square lattice. Henceforth we shall assume that hopping is between nearest neighbors only, uniform and real. The abbreviations $C_2=t^4/(\omega_i-U)^3$ and $\mathcal{S}_{i;j;k}=\mathbf{S}_i\cdot(\mathbf{S}_j \times \mathbf{S}_k)$ will also be used.

To count the two-internal-hop pathways in the square lattice systemically, we fix the initial holon at site 1 and the initial doublon at site 2, and align the coordinates so that $y=0$ for site 1 and 2 and that $\mathbf{x}_{21}=\hat{x}$. All other pathways are clearly related to the ones satisfying the above conditions via symmetries. For the final hop and the initial hop to be noncollinear, a third site not collinear with site 1 and 2 must be involved, and we may further restrict our attention to pathways in which the third site lies in the $y>0$ half plane, since the remaining pathways are related to these via the mirror reflection $y \to -y$.

There are four pathways that satisfy the above restrictions, which are precisely the ones depicted in Fig. 1. Applying the procedures as explained Sec. II, the contributions by these pathways are given by

$$\begin{aligned} T_{2,a} &= C_2 e_i^x (-\bar{e}_f^y)(c_1^\dagger c_3)(c_3^\dagger c_4)(c_4^\dagger c_2)(c_2^\dagger c_1) \\ &= -C_2 e_i^x \bar{e}_f^y \, \mathrm{tr}\{\chi_3 \chi_4 \chi_2 \tilde{\chi}_1\} \\ &\doteq -iC_2 e_i^x \bar{e}_f^y (\mathcal{S}_{3;4;1} + \mathcal{S}_{3;2;1} + \mathcal{S}_{4;2;1} - \mathcal{S}_{3;4;2}), \end{aligned} \quad \text{(A3)}$$

$$\begin{aligned} T_{2,b} &= C_2 e_i^x \bar{e}_f^y (c_4^\dagger c_2)(c_3^\dagger c_4)(c_1^\dagger c_3)(c_2^\dagger c_1) \\ &= C_2 e_i^x \bar{e}_f^y \, \mathrm{tr}\{\chi_2 \tilde{\chi}_1 \tilde{\chi}_3 \tilde{\chi}_4\} \\ &\doteq iC_2 e_i^x \bar{e}_f^y (\mathcal{S}_{1;3;4} - \mathcal{S}_{2;3;4} - \mathcal{S}_{4;2;1} - \mathcal{S}_{2;1;3}), \end{aligned} \quad \text{(A4)}$$

$$\begin{aligned} T_{2,c} &= C_2 e_i^x (-\bar{e}_f^y)(c_2^\dagger c_4)(c_1^\dagger c_2)(c_4^\dagger c_2)(c_2^\dagger c_1) \\ &= -C_2 e_i^x \bar{e}_f^y [(c_4 c_1^\dagger)(c_4^\dagger c_2)(c_2^\dagger c_1) + (c_4 c_4^\dagger)(c_1^\dagger c_2)(c_2^\dagger c_1)] \\ &= -C_2 e_i^x \bar{e}_f^y (\mathrm{tr}\{(-1)\chi_4 \chi_2 \tilde{\chi}_1\} + \mathrm{tr}\{\chi_4\}\mathrm{tr}\{\chi_2 \tilde{\chi}_1\}) \\ &\doteq -2iC_2 i e_i^x \bar{e}_f^y \mathcal{S}_{4;2;1}, \end{aligned} \quad \text{(A5)}$$

$$\begin{aligned} T_{2,d} &= C_2 e_i^x \bar{e}_f^y (c_3^\dagger c_1)(c_1^\dagger c_2)(c_1^\dagger c_3)(c_2^\dagger c_1) \\ &= C_2 e_i^x \bar{e}_f^y [(c_3^\dagger c_2)(c_1^\dagger c_3)(c_2^\dagger c_1) + (c_3^\dagger c_3)(c_1^\dagger c_2)(c_2^\dagger c_1)] \\ &= C_2 e_i^x \bar{e}_f^y (\mathrm{tr}\{(-1)\tilde{\chi}_3 \chi_2 \tilde{\chi}_1\} + \mathrm{tr}\{\tilde{\chi}_3\}\mathrm{tr}\{\chi_2 \tilde{\chi}_1\}) \\ &\doteq 2iC_2 i e_i^x \bar{e}_f^y \mathcal{S}_{3;2;1}. \end{aligned} \quad \text{(A6)}$$

Summing all four terms, we found that $T_{2,a}+T_{2,b}+T_{2,c}+T_{2,d} \doteq 0$. Hence, for the square lattice with only nearest-neighbor hopping, the operator that corresponds to the Raman transition in the A_{2g} channel, $O_{A_{2g}}$, vanishes to the $t^4/(\omega_i-U)^3$ order.

Notice that the orthogonality between the $\hat{x}$ and $\hat{y}$ has not been invoked in the above derivation. Consequently, the above derivation carries to the triangular lattice upon mapping $\hat{x}$ and $\hat{y}$ in the square lattice to any two of bond directions in the triangular lattice. See Fig. 14 for illustration. It can be checked that all two-internal-hop pathways with noncollinear initial and final hops in the triangular lattice can be obtained from such mappings and that there is no issue of double counting. Hence, we conclude that $O_{A_{2g}}$ vanishes up to the $t^4/(\omega_i-U)^3$ order in the triangular lattice also.

Evidently, the criterion that any three noncollinear nearest-neighbor sites belong to a four-site loop is a crucial ingredient for the cancellations of the two-internal-hop contributions as seen above. This criterion is not met in the

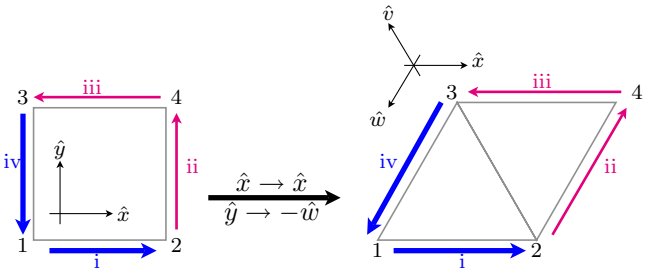

FIG. 14. (Color online) Mapping between the pathways in the square lattice and the pathways in the triangular lattice.

honeycomb lattice or in the kagome lattice. Hence, $O_{A_{2g}}$ may not vanish in these lattices at the $t^4/(\omega_i - U)^3$ order.

First consider the honeycomb lattice, which is shown in Fig. 15, wherein the site labels i, j, the unit vectors $\hat{x}$, $\hat{v}$, $\hat{w}$ along bond directions, and the primitive lattice vectors $\mathbf{a}_1$, $\mathbf{a}_2$, are defined. For an initial holon at i and an initial doublon at j, there are four two-internal-hop pathways, listed in Fig. 16. Summing up their contributions, we get

$$T_{2,i,j} \doteq 2iC_2(-e_i^x \bar{e}_f^w \mathcal{S}_{i+\mathbf{a}_1;j;i} + e_i^x \bar{e}_f^v \mathcal{S}_{j-\mathbf{a}_2;j;i} - e_i^x \bar{e}_f^v \mathcal{S}_{i+\mathbf{a}_2;j;i} + e_i^x \bar{e}_f^w \mathcal{S}_{j-\mathbf{a}_1;j;i}). \quad \text{(A7)}$$

If the initial doublon is fixed at $j-\mathbf{a}_2$ or $j-\mathbf{a}_1$ instead, the contributions are, respectively,

$$T_{2,i,j-\mathbf{a}_2} \doteq 2iC_2(-e_i^v \bar{e}_f^x \mathcal{S}_{i-\mathbf{a}_2;j-\mathbf{a}_2;i} + e_i^v \bar{e}_f^w \mathcal{S}_{j-\mathbf{a}_1;j-\mathbf{a}_2;i} - e_i^v \bar{e}_f^w \mathcal{S}_{i+\mathbf{a}_1-\mathbf{a}_2;j-\mathbf{a}_2;i} + e_i^v \bar{e}_f^x \mathcal{S}_{j;j-\mathbf{a}_2;i}), \quad \text{(A8)}$$

$$T_{2,i,j-\mathbf{a}_1} \doteq 2iC_2(-e_i^w \bar{e}_f^v \mathcal{S}_{i+\mathbf{a}_2-\mathbf{a}_1;j-\mathbf{a}_1;i} + e_i^w \bar{e}_f^x \mathcal{S}_{j;j-\mathbf{a}_1;i} - e_i^w \bar{e}_f^x \mathcal{S}_{i-\mathbf{a}_1;j-\mathbf{a}_1;i} + e_i^w \bar{e}_f^v \mathcal{S}_{j-\mathbf{a}_2;j-\mathbf{a}_1;i}). \quad \text{(A9)}$$

And the analog of Eqs. (A7)–(A9), when the holon is fixed at j, are given by

$$T_{2,j,i} \doteq 2iC_2(-e_i^x \bar{e}_f^w \mathcal{S}_{j-\mathbf{a}_1;j;i} + e_i^x \bar{e}_f^v \mathcal{S}_{i+\mathbf{a}_2;j;i} - e_i^x \bar{e}_f^v \mathcal{S}_{j-\mathbf{a}_2;j;i} + e_i^x \bar{e}_f^w \mathcal{S}_{i+\mathbf{a}_1;j;i}), \quad \text{(A10)}$$

$$T_{2,j,i+\mathbf{a}_2} \doteq 2iC_2(-e_i^v \bar{e}_f^x \mathcal{S}_{j+\mathbf{a}_2;i+\mathbf{a}_2;j} + e_i^v \bar{e}_f^w \mathcal{S}_{i+\mathbf{a}_1;i+\mathbf{a}_2;j} - e_i^v \bar{e}_f^w \mathcal{S}_{j+\mathbf{a}_2-\mathbf{a}_1;i+\mathbf{a}_2;j} + e_i^v \bar{e}_f^x \mathcal{S}_{i;i+\mathbf{a}_2;j}), \quad \text{(A11)}$$

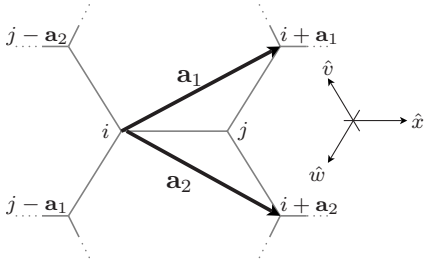

FIG. 15. The honeycomb lattice (thin gray lines), wherein the site label i, j, the unit vectors $\hat{x}$, $\hat{v}$, $\hat{w}$ (thin black arrows), and the primitive lattice vector (thick black arrows), are defined.

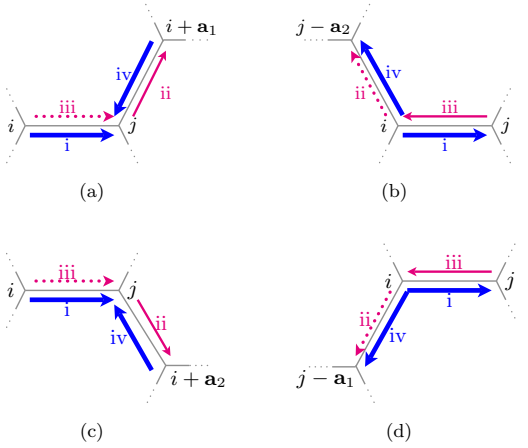

FIG. 16. (Color online) Pathways with two internal hops that contribute to the A_{2g} channel in the honeycomb lattice with the initial holon fixed at site i and initial doublon fixed at site j.

$$T_{2,j,i+\mathbf{a}_1} \doteq 2iC_2(-e_i^w \bar{e}_f^v \mathcal{S}_{j+\mathbf{a}_1-\mathbf{a}_2;i+\mathbf{a}_1;j} + e_i^w \bar{e}_f^x \mathcal{S}_{i;i+\mathbf{a}_1;j} - e_i^w \bar{e}_f^x \mathcal{S}_{j+\mathbf{a}_1;i+\mathbf{a}_1;j} + e_i^w \bar{e}_f^v \mathcal{S}_{i+\mathbf{a}_2;i+\mathbf{a}_1;j}). \quad \text{(A12)}$$

Summing Eqs. (A7)–(A12) over all lattice vectors $\{\mathbf{R}\}$, and reorganize slightly, we finally obtain,

$$T_{2,\mathrm{hex}} \doteq 4iC_2 \sum_R \Big((\mathcal{S}_{j;i;i-\mathbf{a}_1} + \mathcal{S}_{i;j;i+\mathbf{a}_1})(e_i^x \bar{e}_f^w - e_i^w \bar{e}_f^x) + (\mathcal{S}_{i-\mathbf{a}_2;i;j} + \mathcal{S}_{i+\mathbf{a}_2;j;i})(e_i^v \bar{e}_f^x - e_i^x \bar{e}_f^v) + (\mathcal{S}_{j-\mathbf{a}_1;i;i-\mathbf{a}_2} + \mathcal{S}_{i+\mathbf{a}_1;j;i+\mathbf{a}_2})(e_i^w \bar{e}_f^v - e_i^v \bar{e}_f^w) \Big)$$

$$= 4iC_2 \sum_R \Big(\Big(\quad + \quad \Big)(e_i^x \bar{e}_f^w - e_i^w \bar{e}_f^x) + \Big(\quad + \quad \Big)(e_i^v \bar{e}_f^x - e_i^x \bar{e}_f^v) + \Big(\quad + \quad \Big)(e_i^w \bar{e}_f^v - e_i^v \bar{e}_f^w) \Big), \quad \text{(A13)}$$

where graphical symbols are introduced on the second equality to denote the spin-chirality operators. Note that even though the site labels are omitted in the symbols, upon the summation over lattice vectors $\{\mathbf{R}\}$ there is no ambiguity as to which spin-chirality operator a particular symbol is referring to.

Using $e^v = -\frac{1}{2}e^x + \frac{\sqrt{3}}{2}e^y$ and $e^w = -\frac{1}{2}e^x - \frac{\sqrt{3}}{2}e^y$, Eq. (A13) can be converted back to the Cartesian coordinates, which yields

$$T_{2,\mathrm{hex}} \doteq 2\sqrt{3}iC_2 \sum_R (e_i^y \bar{e}_f^x - e_i^x \bar{e}_f^y) \times \Big(\quad + \quad + \quad + \quad + \quad + \quad \Big). \quad \text{(A14)}$$

Finally consider the kagome lattice, which is shown in Fig.

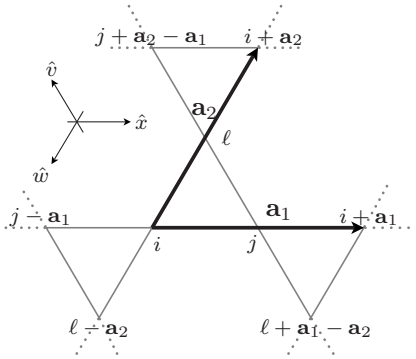

FIG. 17. The kagome lattice (thin gray lines), wherein the site label i, j, the unit vectors $\hat{x}$, $\hat{v}$, $\hat{w}$ (thin black arrows), and the primitive lattice vector (thick black arrows), are defined.

17, wherein the site labels i, j, ℓ, unit vectors $\hat{x}$, $\hat{v}$, $\hat{w}$, and primitive lattice vectors $\mathbf{a}_1$, $\mathbf{a}_2$, are defined. Fixing the initial holon at site i and the initial doublon at site j, four two-internal-hop pathways contribute to the A_{2g} channel (Fig. 18). The sum of their contributions is

$$T_{2,i,j} \doteq 2iC_2\Big(+ e_i^x \bar{e}_f^v \mathcal{S}_{\ell;j;i} - e_i^x \bar{e}_f^w \mathcal{S}_{\ell;j;i} - e_i^x \bar{e}_f^v \mathcal{S}_{\ell+\mathbf{a}_1-\mathbf{a}_2;j;i} + e_i^x \bar{e}_f^w \mathcal{S}_{\ell-\mathbf{a}_2;j;i}\Big)$$
$$= 2iC_2\Big(e_i^x \bar{e}_f^w \Big(\quad + \quad \Big) - e_i^x \bar{e}_f^v \Big(\quad + \quad \Big)\Big), \tag{A15}$$

where graphical symbols are again introduced on the second equality. Note again that upon summing over all lattice vectors {**R**} there is no ambiguity as to which spin-chirality operator a particular symbol refers to.

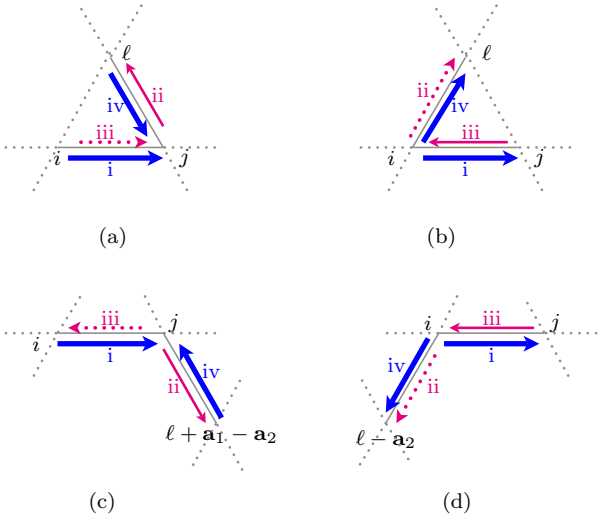

FIG. 18. (Color online) Pathways with two internal hops that contribute to the A_{2g} channel in the kagome lattice with the initial holon fixed at site i and initial doublon fixed at site j.

By changing the site where the initial doublon is located, we get, upon summation, the following contribution to $O_{A_{2g}}$ by two-internal-hop pathways whose initial holon is located at site i,

$$T_{2,i} \doteq 2iC_2\Big(e_i^w \bar{e}_f^v \Big(\quad + \quad + \quad + \quad \Big) - e_i^x \bar{e}_f^v \Big(\quad + \quad + \quad + \quad \Big) + (e_i^x \bar{e}_f^w - e_i^w \bar{e}_f^x)\Big(\quad + \quad + \quad + \quad \Big)\Big). \tag{A16}$$

Obtaining the contributions to $O_{A_{2g}}$ by two-internal-hop pathways whose initial holon is located at site j or ℓ in an analogous manner, we finally get, upon summing over all lattice vectors and basis sites,

$$T_{2,\mathrm{kag}} \doteq 4iC_2 \sum_{\mathbf{R}} \Big((e_i^x \bar{e}_f^w - e_i^w \bar{e}_f^x)\Big(\quad + \quad + \quad + \quad \Big) + (e_i^v \bar{e}_f^x - e_i^x \bar{e}_f^v)\Big(\quad + \quad + \quad + \quad \Big) + (e_i^w \bar{e}_f^v - e_i^v \bar{e}_f^w)\Big(\quad + \quad + \quad + \quad \Big)\Big). \tag{A17}$$

Or, converting back to the Cartesian coordinates,

$$T_{2,\mathrm{kag}} \doteq 2\sqrt{3}iC_2 \sum_{\mathbf{R}} (e_i^y \bar{e}_f^x - e_i^x \bar{e}_f^y)\Big(3 \quad + 3 \quad + \quad + \quad + \quad + \quad + \quad \Big), \tag{A18}$$

which is what we quoted in Eq. (13).

In summary, we found that, with only nearest-neighbor hopping, the A_{2g} channel Raman T matrix does not vanish in the honeycomb lattice or the kagome lattice at the $t^4/(U-\omega_i)^3$ order, but does so to this order in the square lattice and the triangular lattice.

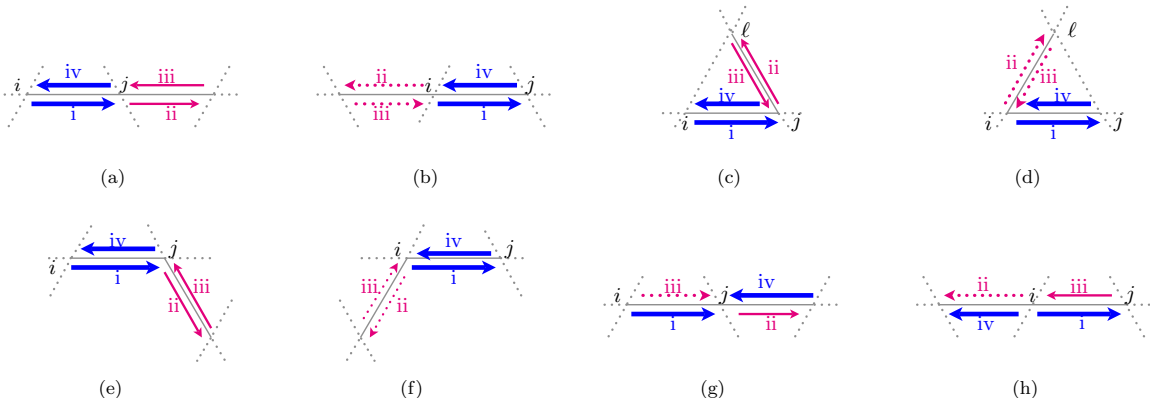

FIG. 19. (Color online) Pathways with two internal hops in a kagome lattice with the initial holon fixed at site i and initial doublon fixed at site j.

APPENDIX B: DERIVATION OF $O_{A_{1g}}$ and O_{E_g} to the $t^4/(\omega_i-U)^3$ order

In this section we shall derive $O_{A_{1g}}$ and O_{E_g} to the $t^4/(\omega_i-U)^3$ order for the kagome lattice. As already noted in Sec. II, at the $t^2/(\omega_i-U)$ order the Shastry-Shraiman formulation reproduces the Fleury-London Hamiltonian. In the A_{1g} channel this gives rise to an operator proportional to the Heisenberg Hamiltonian and in the E_g channel it gives rise to the operators $O_{E_g^{(1)}}$ and $O_{E_g^{(2)}}$ as shown in Eqs. (10) and (11).

At the $t^3/(\omega_i-U)^2$ order, it can be checked that the two types of pathways depicted in Fig. 13 cancel each other not only in the A_{2g} channel but also in the E_g and A_{1g} channels. Thus, it remains to consider pathways having two internal hops, which contributes at the $t^4/(\omega_i-U)^3$ order.

By considering pathways and their "reserved" counterparts, in which all electron operators are conjugated and their order inverted, it is shown in Appendix A that only spin-chirality operators contribute to the A_{2g} channel. From the same construction, it can be seen that the spin-chirality operators *do not* contribute to the E_g and A_{1g} channels. Moreover, we are interested in the inelastic, and hence nonconstant, part of the Raman transition operators. Therefore, to determine the $t^4/(\omega_i-U)^3$ order terms in O_{E_g} and $O_{A_{2g}}$, it suffices to extract the spin dot product terms for each process.

Fixing the initial holon at site i and the initial doublon at site j, there are eight more two-internal-hop pathways that contribute to the A_{1g} and E_g channels in addition to the four depicted in Fig. 18. These are listed in Fig. 19.

Applying the procedures as explained in Sec. II, the spin dot products resulting from Figs. 18(a), 18(b), 19(c), and 19(d) are, respectively,

$$T_{\mathrm{kag},a} = C_2 e_i^x(-\bar{e}_f^v)(\mathrm{tr}\{(-1)\chi_\ell\chi_j\tilde{\chi}_i\} + \mathrm{tr}\{\chi_\ell\}\mathrm{tr}\{\chi_j\tilde{\chi}_i\})$$
$$\doteq C_2 e_i^x(-\bar{e}_f^v)(\mathbf{S}_\ell\cdot\mathbf{S}_i - \mathbf{S}_i\cdot\mathbf{S}_j - \mathbf{S}_j\cdot\mathbf{S}_\ell), \quad \text{(B1)}$$

$$T_{\mathrm{kag},b} = C_2 e_i^x(-\bar{e}_f^w)(\mathrm{tr}\{(-1)\chi_\ell\chi_j\tilde{\chi}_i\} + \mathrm{tr}\{\chi_\ell\}\mathrm{tr}\{\chi_j\tilde{\chi}_i\})$$
$$\doteq C_2 e_i^x(-\bar{e}_f^w)(\mathbf{S}_j\cdot\mathbf{S}_\ell - \mathbf{S}_i\cdot\mathbf{S}_j - \mathbf{S}_\ell\cdot\mathbf{S}_i), \quad \text{(B2)}$$

$$T_{\mathrm{kag},c} = C_2 e_i^x(-\bar{e}_f^x)(c_i^\dagger c_j)(c_j^\dagger c_\ell)(c_\ell^\dagger c_j)(c_j^\dagger c_i)$$
$$= C_2 e_i^x(-\bar{e}_f^x)\mathrm{tr}\{\tilde{\chi}_\ell\}\mathrm{tr}\{\chi_j\tilde{\chi}_i\}$$
$$\doteq -2C_2 e_i^x(-\bar{e}_f^x)\mathbf{S}_i\cdot\mathbf{S}_j, \quad \text{(B3)}$$

$$T_{\mathrm{kag},d} = C_2 e_i^x(-\bar{e}_f^x)(c_i^\dagger c_j)(c_\ell^\dagger c_i)(c_i^\dagger c_\ell)(c_j^\dagger c_i)$$
$$= C_2 e_i^x(-\bar{e}_f^x)\mathrm{tr}\{\chi_\ell\}\mathrm{tr}\{\chi_j\tilde{\chi}_i\} \doteq -2C_2 e_i^x(-\bar{e}_f^x)\mathbf{S}_i\cdot\mathbf{S}_j, \quad \text{(B4)}$$

where $\doteq$ denotes equality upon neglecting additive constants and spin-chirality terms. The contributions of other pathways in Figs. 18 and 19 can be obtained by relabeling sites and vectors that appear in Eqs. (B1)–(B4).

The sum over all pathways in Figs. 18 and 19 gives

$$T_{\mathrm{kag},i,j} \doteq C_2[e_i^x\bar{e}_f^x(\mathbf{S}_i\cdot\mathbf{S}_{j-\mathbf{a}_1} + \mathbf{S}_j\cdot\mathbf{S}_{i+\mathbf{a}_1} + 14\mathbf{S}_i\cdot\mathbf{S}_j - \mathbf{S}_i\cdot\mathbf{S}_{i+\mathbf{a}_1}$$
$$- \mathbf{S}_j\cdot\mathbf{S}_{j-\mathbf{a}_1}) + e_i^x\bar{e}_f^v(\mathbf{S}_i\cdot\mathbf{S}_{\ell+\mathbf{a}_1-\mathbf{a}_2} + \mathbf{S}_j\cdot\mathbf{S}_\ell - \mathbf{S}_i\cdot\mathbf{S}_\ell$$
$$- \mathbf{S}_j\cdot\mathbf{S}_{\ell+\mathbf{a}_1-\mathbf{a}_2}) + e_i^x\bar{e}_f^w(\mathbf{S}_j\cdot\mathbf{S}_{\ell-\mathbf{a}_2} + \mathbf{S}_i\cdot\mathbf{S}_\ell - \mathbf{S}_j\cdot\mathbf{S}_\ell$$
$$- \mathbf{S}_i\cdot\mathbf{S}_{\ell-\mathbf{a}_2})]. \quad \text{(B5)}$$

The contributions when the initial holon and/or the initial doublon are located at other sites can be obtained by relabeling. The sum over the locations of the initial holon and the initial doublon yields

$$T_{\mathrm{kag}} \doteq 2C_2\sum_{\{\mathbf{R}\}}[e_i^x\bar{e}_f^x(16\mathbf{S}_i\cdot\mathbf{S}_j + 16\mathbf{S}_j\cdot\mathbf{S}_{i+\mathbf{a}_1} - 2\mathbf{S}_i\cdot\mathbf{S}_{i+\mathbf{a}_1}$$
$$- 2\mathbf{S}_j\cdot\mathbf{S}_{j-\mathbf{a}_1}) + e_i^v\bar{e}_f^v(16\mathbf{S}_j\cdot\mathbf{S}_\ell + 16\mathbf{S}_\ell\cdot\mathbf{S}_{j+\mathbf{a}_2-\mathbf{a}_1}$$
$$- 2\mathbf{S}_j\cdot\mathbf{S}_{j+\mathbf{a}_2-\mathbf{a}_1} - 2\mathbf{S}_\ell\cdot\mathbf{S}_{\ell+\mathbf{a}_2-\mathbf{a}_1}) + e_i^w\bar{e}_f^w(16\mathbf{S}_i\cdot\mathbf{S}_\ell$$
$$+ 16\mathbf{S}_\ell\cdot\mathbf{S}_{i+\mathbf{a}_2} - 2\mathbf{S}_i\cdot\mathbf{S}_{i+\mathbf{a}_2} - 2\mathbf{S}_\ell\cdot\mathbf{S}_{\ell+\mathbf{a}_2})$$
$$+ (e_i^x\bar{e}_f^w + e_i^w\bar{e}_f^x)(\mathbf{S}_j\cdot\mathbf{S}_{\ell-\mathbf{a}_2} + \mathbf{S}_\ell\cdot\mathbf{S}_{j-\mathbf{a}_1} - \mathbf{S}_j\cdot\mathbf{S}_\ell$$
$$- \mathbf{S}_{\ell-\mathbf{a}_2}\cdot\mathbf{S}_{j-\mathbf{a}_1}) + (e_i^x\bar{e}_f^v + e_i^v\bar{e}_f^x)(\mathbf{S}_i\cdot\mathbf{S}_{\ell+\mathbf{a}_1-\mathbf{a}_2} + \mathbf{S}_\ell\cdot\mathbf{S}_{j+\mathbf{a}_1}$$
$$- \mathbf{S}_i\cdot\mathbf{S}_\ell - \mathbf{S}_{\ell+\mathbf{a}_1-\mathbf{a}_2}\cdot\mathbf{S}_{j+\mathbf{a}_1}) + (e_i^v\bar{e}_f^w + e_i^w\bar{e}_f^v)(\mathbf{S}_i\cdot\mathbf{S}_{j+\mathbf{a}_2-\mathbf{a}_1}$$
$$+ \mathbf{S}_j\cdot\mathbf{S}_{i+\mathbf{a}_2} - \mathbf{S}_i\cdot\mathbf{S}_j - \mathbf{S}_{j+\mathbf{a}_2-\mathbf{a}_1}\cdot\mathbf{S}_{i+\mathbf{a}_2})]. \quad \text{(B6)}$$

Projecting onto the A_{1g} channel and neglecting a piece proportional to the Heisenberg Hamiltonian yields Eq. (12) while projecting into the E_g channels yields the following contributions to $O_{E_g^{(1)}}$ and $O_{E_g^{(2)}}$ at the $t^4/(\omega_i - U)^3$ order, respectively,

$$\begin{aligned}\delta O_{E_g^{(1)}} = C_2[&(2\mathbf{S}_i\cdot\mathbf{S}_{j+\mathbf{a}_2-\mathbf{a}_1} + 2\mathbf{S}_j\cdot\mathbf{S}_{i+\mathbf{a}_2} - \mathbf{S}_j\cdot\mathbf{S}_{\ell-\mathbf{a}_2} - \mathbf{S}_\ell\cdot\mathbf{S}_{j-\mathbf{a}_1} - \mathbf{S}_i\cdot\mathbf{S}_{\ell+\mathbf{a}_1-\mathbf{a}_2} - \mathbf{S}_\ell\cdot\mathbf{S}_{j+\mathbf{a}_1})\\ &- (2\mathbf{S}_i\cdot\mathbf{S}_{i+\mathbf{a}_1} + 2\mathbf{S}_j\cdot\mathbf{S}_{j-\mathbf{a}_1} - \mathbf{S}_i\cdot\mathbf{S}_{i+\mathbf{a}_2} - \mathbf{S}_\ell\cdot\mathbf{S}_{\ell+\mathbf{a}_2} - \mathbf{S}_j\cdot\mathbf{S}_{j+\mathbf{a}_2-\mathbf{a}_1} - \mathbf{S}_\ell\cdot\mathbf{S}_{\ell+\mathbf{a}_2-\mathbf{a}_1})\\ &+ 7(2\mathbf{S}_i\cdot\mathbf{S}_j + 2\mathbf{S}_j\cdot\mathbf{S}_{i+\mathbf{a}_1} - \mathbf{S}_i\cdot\mathbf{S}_\ell - \mathbf{S}_\ell\cdot\mathbf{S}_{i+\mathbf{a}_2} - \mathbf{S}_j\cdot\mathbf{S}_\ell - \mathbf{S}_\ell\cdot\mathbf{S}_{j+\mathbf{a}_2-\mathbf{a}_1})],\end{aligned} \tag{B7}$$

$$\begin{aligned}\delta O_{E_g^{(2)}} = \sqrt{3}C_2[&(\mathbf{S}_j\cdot\mathbf{S}_{\ell-\mathbf{a}_2} + \mathbf{S}_\ell\cdot\mathbf{S}_{j-\mathbf{a}_1} - \mathbf{S}_i\cdot\mathbf{S}_{\ell+\mathbf{a}_1-\mathbf{a}_2} - \mathbf{S}_\ell\cdot\mathbf{S}_{j+\mathbf{a}_1}) - (\mathbf{S}_i\cdot\mathbf{S}_{i+\mathbf{a}_2} + \mathbf{S}_\ell\cdot\mathbf{S}_{\ell+\mathbf{a}_2} - \mathbf{S}_j\cdot\mathbf{S}_{j+\mathbf{a}_2-\mathbf{a}_1} - \mathbf{S}_\ell\cdot\mathbf{S}_{\ell+\mathbf{a}_2-\mathbf{a}_1})\\ &+ 7(\mathbf{S}_i\cdot\mathbf{S}_\ell + \mathbf{S}_\ell\cdot\mathbf{S}_{i+\mathbf{a}_2} - \mathbf{S}_j\cdot\mathbf{S}_\ell - \mathbf{S}_\ell\cdot\mathbf{S}_{j+\mathbf{a}_2-\mathbf{a}_1})].\end{aligned} \tag{B8}$$

As explained in Sec. IV, it can be checked that $\delta O_{E_g^{(1)}}$ and $\delta O_{E_g^{(2)}}$ in the above equations do not produce any transition in the Dirac Hamiltonian (20).

[1] J. S. Helton, K. Matan, M. P. Shores, E. A. Nytko, B. M. Bartlett, Y. Yoshida, Y. Takano, A. Suslov, Y. Qiu, J.-H. Chung, D. G. Nocera, and Y. S. Lee, Phys. Rev. Lett. **98**, 107204 (2007).

[2] P. Mendels, F. Bert, M. A. de Vries, A. Olariu, A. Harrison, F. Duc, J. C. Trombe, J. S. Lord, A. Amato, and C. Baines, Phys. Rev. Lett. **98**, 077204 (2007).

[3] O. Ofer, A. Keren, E. A. Nytko, M. P. Shores, B. M. Bartlett, D. G. Nocera, C. Baines, A. Amato arXiv:cond-mat/0610540 (unpublished).

[4] M. P. Shores, E. A. Nytko, B. M. Bartlett, and D. G. Nocera, J. Am. Chem. Soc. **127**, 13462 (2005).

[5] M. A. de Vries, K. V. Kamenev, W. A. Kockelmann, J. Sanchez-Benitez, and A. Harrison, Phys. Rev. Lett. **100**, 157205 (2008).

[6] F. Bert, S. Nakamae, F. Ladieu, D. L'Hôte, P. Bonville, F. Duc, J.-C. Trombe, and P. Mendels, Phys. Rev. B **76**, 132411 (2007).

[7] S.-H. Lee, H. Kikuchi, Y. Qiu, B. Lake, Q. Huang, K. Habicht, and K. Kiefer, Nature Mater. **6**, 853 (2007).

[8] A. Olariu, P. Mendels, F. Bert, F. Duc, J. C. Trombe, M. A. de Vries, and A. Harrison, Phys. Rev. Lett. **100**, 087202 (2008).

[9] T. Imai, E. A. Nytko, B. M. Bartlett, M. P. Shores, and D. G. Nocera, Phys. Rev. Lett. **100**, 077203 (2008).

[10] M. B. Hastings, Phys. Rev. B **63**, 014413 (2000).

[11] P. Nikolic and T. Senthil, Phys. Rev. B **68**, 214415 (2003).

[12] Y. Ran, M. Hermele, P. A. Lee, and X.-G. Wen, Phys. Rev. Lett. **98**, 117205 (2007).

[13] O. Cepas, J. O. Haerter, and C. Lhuillier, Phys. Rev. B **77**, 172406 (2008).

[14] M. Hermele, Y. Ran, P. A. Lee, and X.-G. Wen, Phys. Rev. B **77**, 224413 (2008).

[15] B. S. Shastry and B. I. Shraiman, Phys. Rev. Lett. **65**, 1068 (1990).

[16] B. S. Shastry and B. I. Shraiman, Int. J. Mod. Phys. B **5**, 365 (1991).

[17] This introduces a small nuance that $\mathcal{E}_i$ can no longer be treated as a scalar but must be considered as a matrix that depends on the initial and final spin states (but independent of the intermediate states). However, the off-diagonal terms of this matrix is of order t/U and hence negligible.

[18] P. A. Fleury and R. Loudon, Phys. Rev. **166**, 514 (1968).

[19] P. E. Sulewski, P. A. Fleury, K. B. Lyons, and S.-W. Cheong, Phys. Rev. Lett. **67**, 3864 (1991).

[20] F. Bert, A. Olariu, A. Zorko, P. Mendels, J. C. Trombe, F. Duc, M. A. de Vries, A. Harrison, A. D. Hillier, J. Lord, A. Amato, and C. Baines,J. Phys.: Conf. Ser. **145**, 012004 (2009).

[21] G. Baskaran, Z. Zou, and P. W. Anderson, Solid State Commun. **63**, 973 (1987).

[22] G. Kotliar and J. Liu, Phys. Rev. B **38**, 5142 (1988).

[23] To perform the analytic calculations, the expectation $\langle f_i^\dagger f_j\rangle$ for next- and next-next-nearest neighbors are needed. From the DSL ansatz these must be real, equal in magnitude, but vary in signs. We determine the signs using numerical calculations as a shortcut. It turns out that the cancellation holds separately for next-nearest neighbor terms and next-next-nearest ones. Thus the determination of signs is adequate for reaching our conclusion.

[24] Since the photon momentum is small, we can ignore distances at the lattice scale. Thus, the precise definition of $\mathbf{r}_{ijk}$ do not concern us.

[25] L. B. Ioffe and A. I. Larkin, Phys. Rev. B **39**, 8988 (1989).

[26] D. Wulferding and P. Lemmens (unpublished).